DRUG DEVELOPMENT

Phenotypic screening with deep learning identifies HDAC6 inhibitors as cardioprotective in a BAG3 mouse model of dilated cardiomyopathy

Jin Yang[1], Francis Grafton[1], Sara Ranjbarvaziri[1], Ana Budan[1], Farshad Farshidfar[1], Marie Cho[1], Emma Xu[1], Jaclyn Ho[1], Mahnaz Maddah[2], Kevin E. Loewke[2], Julio Medina[3], David Sperandio[3], Snahel Patel[1], Tim Hoey[1], Mohammad A. Mandegar[1]*

Dilated cardiomyopathy (DCM) is characterized by reduced cardiac output, as well as thinning and enlargement of left ventricular chambers. These characteristics eventually lead to heart failure. Current standards of care do not target the underlying molecular mechanisms associated with genetic forms of heart failure, driving a need to develop novel therapeutics for DCM. To identify candidate therapeutics, we developed an in vitro DCM model using induced pluripotent stem cell–derived cardiomyocytes (iPSC-CMs) deficient in B-cell lymphoma 2 (BCL2)-associated athanogene 3 (BAG3). With these BAG3-deficient iPSC-CMs, we identified cardioprotective drugs using a phenotypic screen and deep learning. From a library of 5500 bioactive compounds and siRNA validation, we found that inhibiting histone deacetylase 6 (HDAC6) was cardioprotective at the sarcomere level. We translated this finding to a BAG3 cardiomyocyte–knockout (BAG3^cKO) mouse model of DCM, showing that inhibiting HDAC6 with two isoform-selective inhibitors (tubastatin A and a novel inhibitor TYA-018) protected heart function. In BAG3^cKO and BAG3^E455K mice, HDAC6 inhibitors improved left ventricular ejection fraction and reduced left ventricular diameter at diastole and systole. In BAG3^cKO mice, TYA-018 protected against sarcomere damage and reduced Nppb expression. Based on integrated transcriptomics and proteomics and mitochondrial function analysis, TYA-018 also enhanced energetics in these mice by increasing expression of targets associated with fatty acid metabolism, protein metabolism, and oxidative phosphorylation. Our results demonstrate the power of combining iPSC-CMs with phenotypic screening and deep learning to accelerate drug discovery, and they support developing novel therapies that address underlying mechanisms associated with heart disease.

INTRODUCTION

Dilated cardiomyopathy (DCM) is a form of heart muscle weakness characterized by reduced cardiac output, as well as thinning and enlargement of left ventricular chambers (1, 2). DCM affects about 1 of 2500 adults (2), accounts for 30 to 40% of all heart failure cases in clinical trials, and is a major cause of heart transplants (1, 3). Current treatments for heart failure include angiotensin-converting enzyme inhibitors, angiotensin receptor blockers, beta-blockers, aldosterone antagonists, vasodilators, angiotensin receptor–neprilysin inhibitors, and sodium-glucose cotransporter 2 inhibitors. However, these treatments mainly ameliorate symptoms and do not target the underlying molecular mechanisms associated with genetic forms of heart failure (4). Therefore, we critically need therapeutics that precisely target the genetic causes of heart failure and prevent worsening function of cardiac muscle (5).

About one-third of individuals with DCM have an inherited form of the disease. Familial DCM accounts for 30 to 50% of all DCM cases and has an autosomal-dominant mode of inheritance (1). Genetic forms of DCM have been associated with more than 50 genes, and more than 50% of patients with DCM have at least one mutation in one of these genes (1, 2). Several of these DCM-associated genes code for central regulators of protein quality control, and mutations in these genes lead to protein aggregation and accumulation of misfolded proteins (6, 7).

One gene that is essential to maintaining protein quality control is B-cell lymphoma 2 (BCL2)-associated athanogene 3 (BAG3). BAG3 is a stress response gene, and it acts as a heat shock protein 70 (HSP70) co-chaperone in a complex with small HSPs to maintain cardiomyocyte function (8–12). BAG3 is highly expressed in cardiac and skeletal muscle, and it can localize to the Z-disk (13). BAG3 has also been proposed to protect myocytes from mechanical damage and proteotoxic stress (9, 14).

Mutations in BAG3 have been linked to DCM. In adults over 40 years old, loss-of-function BAG3 mutations show 80% penetrance in DCM (1, 2). Familial BAG3 mutations are autosomal dominant, suggesting a heterozygous loss-of-function mechanism (2, 9, 15). BAG3 mutations that result in BAG3 loss of function account for ~3% of variant distribution in DCM genes (16). Most mutations in BAG3 are deleterious (e.g., E455K), but a cardioprotective variant (C151R) has also been reported (2). This finding suggests that the BAG3 chaperone complex may acquire a gain-of-function phenotype that protects against proteotoxic stress and mechanical damage in the heart. In addition, mutations in BAG3 led to cardiac-related phenotypes both in vivo and in vitro, in zebrafish (17, 18), mice (6, 13), and human induced pluripotent stem cell–derived cardiomyocytes (iPSC-CMs) (9). In the BAG3 mouse models (6), cardiac output shows a steady decline, which creates an ideal window of opportunity to intervene with a small molecule. Moreover, BAG3 expression was reduced in patients with idiopathic DCM, implying that BAG3 must be expressed at certain amounts to maintain its chaperone function in protein quality control (19, 20). Therefore, BAG3 is an attractive target for developing small-molecule therapeutics for

[1]Tenaya Therapeutics, South San Francisco, CA 94080, USA. [2]Dana Solutions, Palo Alto, CA 94306, USA. [3]R2M Pharma, South San Francisco, CA 94080, USA.
*Corresponding author. Email: mandegar@gmail.com

Yang et al., Sci. Transl. Med. 14, eabl5654 (2022) 6 July 2022

1 of 15

BAG3 myopathies. These efforts could also lead to interventions for other genetic causes of DCM and nongenetic forms of heart failure (*7*).

In this study, we aimed to identify small-molecule therapeutic targets for BAG3-related DCM that could enable drug development for genetically defined cardiomyopathies that disrupt protein quality control. Previously, we showed the feasibility of high-content phenotypic screening using deep learning with iPSC-CMs (*21*). We hypothesized that we could use a similar approach to identify cardioprotective small-molecule targets in BAG3-deficient iPSC-CMs that would translate to therapeutic benefits in a mouse model of DCM.

RESULTS
Loss of BAG3 in iPSC-CMs leads to sarcomere damage
To develop a robust and reproducible loss-of-function model of DCM, we expressed small interfering RNAs (siRNAs) targeting *BAG3* in human iPSC-CMs. First, using scramble (SCR) siRNA labeled with red fluorescent protein, we optimized conditions for iPSC-CM seeding density and transfection to ensure more than 95% transfection efficiency (fig. S1A). Next, using a pool of four siRNAs targeting *BAG3*, we obtained ~90% knockdown of *BAG3* mRNA in iPSC-CMs as measured using quantitative polymerase chain reaction (qPCR; Fig. 1A) and RNA sequencing (RNA-seq; fig. S1B). We also showed that the quantity of BAG3 protein was reduced by 70 to 90% using Western blot, flow cytometry, and immunostaining (Fig. 1, B and C, and fig. S1, C to E). BAG3 knockdown (BAG3^{KD}) in iPSC-CMs remained suppressed for at least 10 days after transfection. This finding is likely due to the low proliferative capacity of iPSC-CMs that prevents siRNA dilution after transfection. Unlike the previously described BAG3^{KO} iPSC-CM models (*9*), we found that the BAG3-siRNA knockdown model showed stronger and more consistent sarcomere damage and reduced batch-to-batch experimental variability. In addition, our model using BAG3 siRNA was amenable to high-content screening because it provided the ideal dynamic range to enable robust hit identification (fig. S2).

Given the central role of BAG3 in maintaining protein quality control, we looked at the quantity of proteins in the BAG3 chaperone complex. In particular, the protein HSPB8 forms a stoichiometric complex with BAG3, and its stability depends on this association (*11*). Compared to SCR iPSC-CMs, BAG3^{KD} iPSC-CMs expressed less HSPB8 (Fig. 1B), suggesting destabilization of the BAG3 chaperone complex. We also assessed p62, a ubiquitin-binding protein (coded by the *SQSTM1* gene) that targets damaged proteins for clearance through the autophagosome (*22*). Compared to SCR iPSC-CMs, BAG3^{KD} iPSC-CMs showed lower expression of p62 (Fig. 1, B and C), suggesting defects in sarcomere integrity and autophagic flux. We further assessed sarcomere integrity by evaluating cardiac myosin-binding protein C (MYBPC3) staining. MYBPC3 is a cardiomyocyte-specific protein that localizes to the C-zone of the sarcomere (*23*), and its content and localization highly depend on sarcomere integrity. MYBPC3 also interacts with BAG3 (*9*). In BAG3^{KD} iPSC-CMs, protein expression of MYBPC3 was unchanged when measured with Western blot (Fig. 1B); however, they were reduced by ~25% ($P < 0.0001$) when measured with immunostaining (Fig. 1C). Immunostaining of MYBPC3 revealed sarcomere damage in BAG3^{KD} iPSC-CMs (Fig. 1, D and E).

To identify the best time for screening after knockdown, we looked at the extent of sarcomere damage in BAG3^{KD} iPSC-CMs. We manually scored sarcomeres [described in the manual sarcomere scoring method of the Supplemental Materials and Methods (*9*, *24*)] and

found that the percentage of damaged sarcomeres increased over time (Fig. 1D). Figure 1E shows representative immunostaining of iPSC-CMs treated with SCR or BAG3 siRNA. The arrows indicate breaks and reduced sarcomere content in BAG3^{KD} iPSC-CMs.

Deep learning reproducibly and accurately identifies healthy and diseased cellular phenotypes
To efficiently and reproducibly quantify sarcomere damage in BAG3^{KD} iPSC-CMs, we adopted an imaging analysis method that uses deep learning (*25*). As we previously described (*21*), we used a two-class deep learning model based on healthy (SCR siRNA–treated) and diseased (BAG3 siRNA–treated) iPSC-CMs. We labeled about 1300 images from each class of iPSC-CMs and fed them into the neural network (Fig. 2A). In each training, 20% of the images were reserved for validation. Images were passed through a series of nodes in the hidden layer to build a model that identified features that best separate the two classes of cells. This process was repeated 20 times (epochs) until an optimal model was generated. Figure 2B shows representative accuracy plots from three independent studies. In cases with a robust cellular phenotype, the accuracy of the model was greater than 95%. In cases with a mild or variable phenotype, the accuracy of the model was ~70 to 80%. In cases with no phenotype to separate the classes, the accuracy of the model was ~50%, suggesting a random class designation.

To show the high accuracy of deep learning in identifying subtle and undefined features of cells, six members of the laboratory who routinely conduct iPSC-CM assays blindly scored sarcomeres in 100 randomly selected images (50:50 mix of SCR and BAG3 siRNA–treated). They categorized images on the basis of sarcomere damage to either class. Although this approach achieved an average accuracy of 70 to 75% for each class, deep learning achieved more than 99% accuracy (Fig. 2C). We also saw reproducible sarcomere damage in several pilot studies using individual siRNAs targeting BAG3 (fig. S2). In addition, by titrating the concentration of BAG3 siRNA, we identified intermediate amounts of sarcomere damage using the cardiomyocyte score based on deep learning (fig. S2).

High-content phenotypic screening identifies histone deacetylase and microtubule inhibitors as cardioprotective compounds
To identify candidate therapeutics that protect against sarcomere damage, we conducted an unbiased high-content screen using a library of 5500 bioactive compounds. To this end, iPSC-CMs were seeded, allowed to recover, treated with either SCR or BAG3 siRNA, and then treated with the bioactive compounds at a 1 μM concentration (Fig. 2D). Using deep learning, we determined the sarcomere score for each compound. A high sarcomere score indicated low sarcomere damage; a low sarcomere score indicated high sarcomere damage, and a negative sarcomere score indicated that the compound was toxic (Fig. 2E).

We ranked screening results on the basis of the sarcomere score and designated a hit threshold of 0.3 (false discovery rate of 1%). Results from wells treated with either SCR or BAG3 siRNA were plotted as controls. These data showed that cells treated with SCR siRNA had a sarcomere score ranging from 0.3 to 1, whereas cells treated with BAG3 siRNA had a sarcomere score below 0.3. After manually excluding false-positive hits (due to rare staining and imaging artifacts; fig. S3A), we grouped the top 24 hits from the screen into distinct target classes (Fig. 2F). A list of compounds identified in the primary screen is summarized in table S1. The top
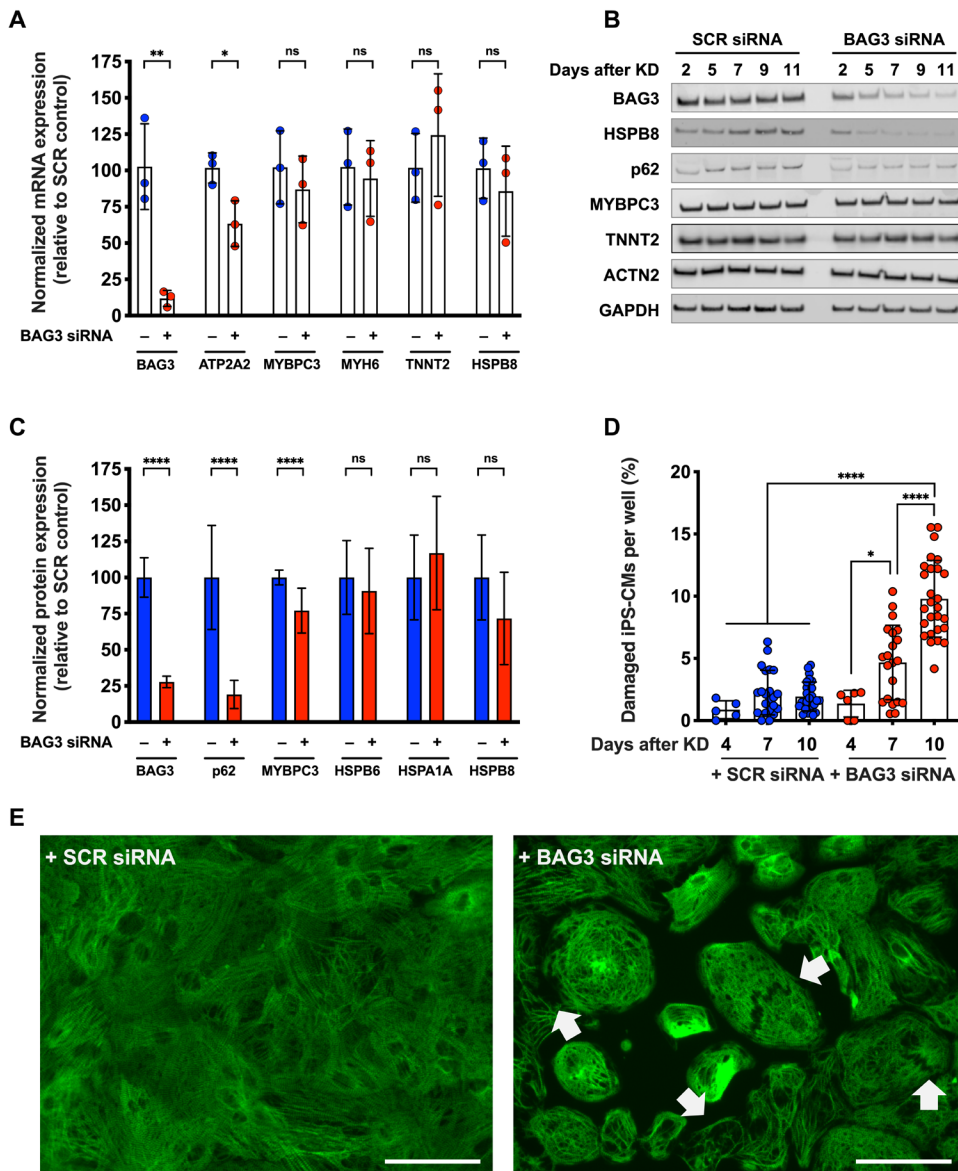
Fig. 1. Development of BAG3 loss-of-function model in iPSC-CMs. (**A**) qPCR analysis of iPSC-CMs treated with SCR or BAG3 siRNA, analyzed 10 days after knockdown. Data were normalized to glyceraldehyde-3-phosphate dehydrogenase (GAPDH) as internal control. (**B**) iPSC-CMs treated with SCR and BAG3 siRNA were harvested 2 to 11 days after treatment. Total protein was extracted from samples and analyzed using Western blot. KD, knockdown. (**C**) Protein quantification using immunostaining of iPSC-CMs treated with SCR and BAG3 siRNA. (**D**) Quantification of sarcomere damage in iPSC-CMs treated with SCR or BAG3 siRNA. (**E**) Representative immunostaining of iPSC-CMs treated with SCR or BAG3 siRNA and then stained with an antibody against MYBPC3. Arrows indicate breaks and reduced sarcomere content in BAG3 knockdown cells. Scale bars, 50 μm. $N > 3$ technical replicates. Data are shown as means ± SD. Multiple comparisons were made using one-way analysis of variance (ANOVA). *$P < 0.05$, **$P < 0.01$, and ****$P < 0.0001$. ns, not significant.

iPSC-CMs and deep learning to identify cardioprotective compounds in an unbiased and high-content manner. Representative immunocytochemistry images from the primary screen are shown in fig. S3B.

HDAC inhibitors do not up-regulate BAG3 expression in iPSC-CMs

Given the abundance of hit enrichment with HDAC inhibitors, we wanted to ensure that HDAC inhibitors did not prevent sarcomere damage by increasing BAG3 expression in wild-type (WT) iPSC-CMs. To capture a broad spectrum of inhibitors, we used all HDAC inhibitors identified from the screen and additional HDAC inhibitors. On the basis of immunostaining and qPCR, none of the HDAC inhibitors increased BAG3 expression in WT iPSC-CMs (fig. S3, C and D). These data suggest that the HDAC inhibitors did not protect against sarcomere damage by preventing BAG3 knockdown or up-regulating BAG3. Instead, they confer cardioprotection through a different mechanism.

HDAC6 inhibition protects against BAG3 loss of function in iPSC-CMs

We performed a secondary validation of the top hits from the primary screen, the results of which are summarized in Fig. 3A. These results highlighted that HDAC and microtubule inhibitors are putative cardioprotective compounds. HDAC inhibitors show varying types of polypharmacology for different HDAC isoforms. For example, class I HDACs (HDAC1, 2, 3, and 8) are predominantly located in the nucleus and target histone substrates. Inhibiting these isoforms activates global or specific gene expression programs (*26*). We further interrogated all HDACs individually using siRNA to co-knockdown BAG3 and individual HDAC isoforms (HDAC1 through HDAC11). In independent studies (two to seven biological replicates), co-knockdown of HDAC6 with BAG3 prevented sarcomere damage induced by BAG3 knockdown as measured by the cardiomyocyte

predicted cardioprotective compounds fell under two major classes: histone deacetylase (HDAC) inhibitors and microtubule inhibitors. Among these, the screen identified three compounds that can be broadly classified as "standard-of-care" agents for cardiovascular indications: omecamtiv mecarbil (cardiac myosin activator), sotalol (beta-blocker and K-channel blocker), and anagrelide [phosphodiesterase 3 (PDE3) inhibitor]. These results validate the translational relevance of using

score (Fig. 3B). Representative immunostainings of BAG3 siRNA–treated cells showed damaged sarcomeres, which appeared reduced by knockdown of HDAC6 (Fig. 3C).

We further validated these findings using siRNAs that independently target HDAC1 through HDAC11. We found that two siRNAs (1 and 3) targeting HDAC6 protected against sarcomere damage in the BAG3[KD] model when used separately or pooled (fig. S4A) and did not affect
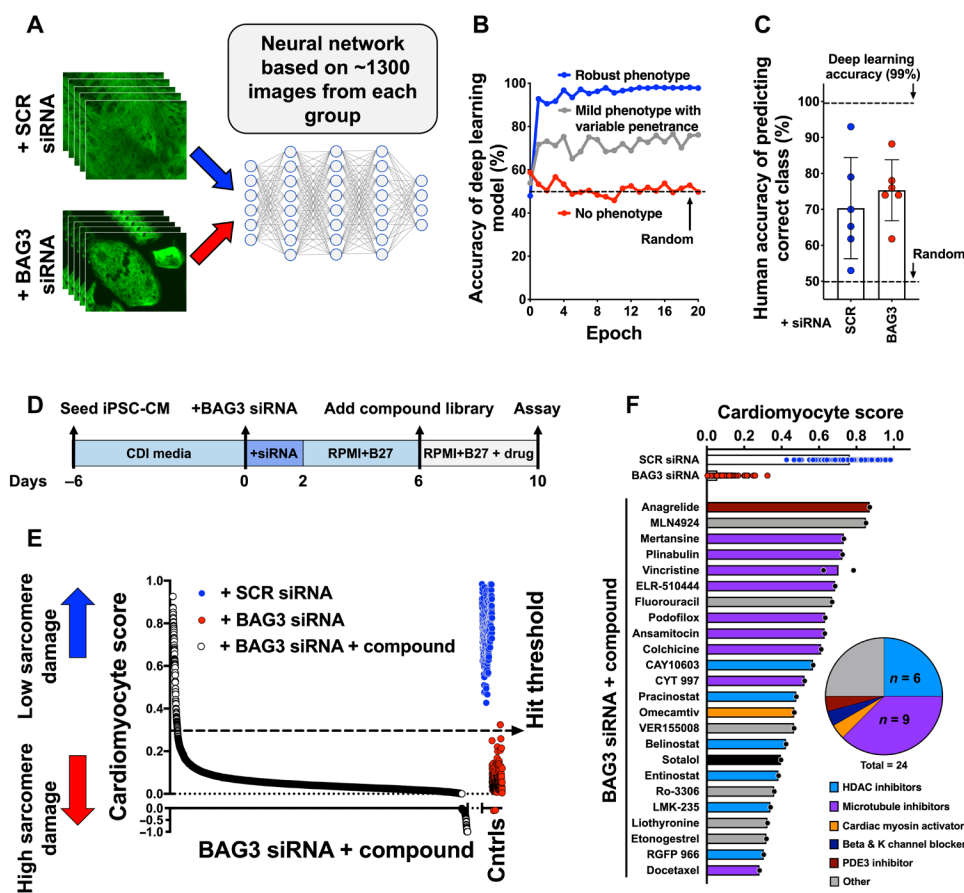
Fig. 2. Phenotypic screening with deep learning identifies HDAC and microtubule inhibitors as putative cardio-protective agents. (**A**) Schematic overview of phenotypic screen model. About 1300 images from each class of iPSC-CMs (treated with SCR or BAG3 siRNA) were labeled and fed into the neural network. Twenty percent of images were used to validate the model. Images were passed through a series of nodes in the hidden layers, building a model that identifies features that best separate the two classes of cells. This process was repeated 20 times (epochs) until an optimal model was generated with a typical validation accuracy of greater than 95%. (**B**) Plot showing accuracy of deep learning models in three different studies (robust, mild, or no strong phenotype). (**C**) Human accuracy to detect subtle phenotypic changes. One hundred images from iPSC-CMs treated with SCR and BAG3 siRNA were blindly scored by six members of the laboratory. The deep learning accuracy (99%) of predicting the correct class is shown as a dashed line. Data are shown as means ± SD. (**D**) Schematic timeline of the high-content screening approach using iPSC-CMs. (**E**) Cardiomyocyte score of sarcomere damage induced by BAG3 siRNA and compounds in iPSC-CMs. An unbiased screen was performed using a library of 5500 bioactive compounds. iPSC-CMs were treated with BAG3 siRNA and compounds at 1 μM. Hits were first identified using deep learning model trained on images from iPSC-CMs treated with either SCR or BAG3 siRNA. The hit threshold was set at a cardiomyocyte score of 0.3. Cntrls, controls. (**F**) The top 24 compounds consisted of HDAC and microtubule inhibitors. In addition, three known heart failure agents were identified: sotalol (beta-blocker and K-channel blocker), omecamtiv mecarbil (cardiac myosin activator), and anagrelide (PDE3 inhibitor).

BAG3 expression (fig. S4B). To further confirm which HDAC is a target for tubulin, we also measured acetylated tubulin (Ac-Tubulin) intensity in these knockdown studies. We found that Ac-Tubulin intensity was significantly greater with knockdown of HDAC3 and HDAC6 versus the SCR control ($P < 0.01$; fig. S4C).

HDAC6 inhibition or knockout leads to tubulin hyperacetylation

Previous studies showed that HDAC6 is located in the cytoplasm (*27, 28*). Here, we verified that HDAC6 is predominantly cytoplasmic (~90%) in iPSC-CMs (fig. S5, A and B). Using CRISPR-Cas9, we generated

HDAC6 knockout (HDAC6^{KO}) iPSCs. We successfully differentiated these cells to cardiomyocytes, as described previously (*21*), which showed expression of sarcomeric markers [cardiac troponin T (TNNT2) and MYBPC3] and hyperacetylation of tubulin (fig. S5, C and D).

Overexpression of HDAC3 and HDAC6 leads to tubulin deacetylation

We overexpressed human HDAC1 through HDAC11 (tagged with a green fluorescent protein reporter at the C-terminal domain) in HDAC6^{KO} iPSC-CMs and measured Ac-Tubulin intensity. Overexpression of HDAC6 in HDAC6^{KO} iPSC-CMs reduced Ac-Tubulin (fig. S5, E and F), confirming that HDAC6 is a tubulin deacetylase (*27*). HDAC6^{KO} iPSC-CMs have about three times higher Ac-Tubulin intensity than HDAC6^{WT} iPSC-CMs. We treated HDAC6^{WT} iPSC-CMs with an HDAC6 inhibitor (tubastatin A), which increased Ac-Tubulin to an intensity similar to HDAC6^{KO} iPSC-CMs (fig. S5G).

TYA-018 is a highly selective HDAC6 inhibitor

Hydroxamic acids are zinc chelators that have been used extensively to develop pan- and HDAC-selective inhibitors. However, hydroxamic acids are known to cause genotoxicity (*29*); in addition, they either lack the desired selectivity or show poor bioavailability with an unfavorable pharmacokinetic profile (*30, 31*). Thus, we developed a novel, exquisitely selective HDAC6 inhibitor (TYA-018) by using a fluoroalkyl oxadiazole as the zinc-binding group (Fig. 4A). We ensured high selectivity of TYA-018 using a biochemical assay and measured potency against HDAC6 and selectivity against HDAC1 (Fig. 4B). As controls, we used a pan-HDAC inhibitor (givinostat) and a well-known HDAC6-specific inhibitor (tubastatin A). Tubastatin A is selective for HDAC6; however, at high concentrations, it has off-target activity with HDAC1, HDAC8 (*30*), and HDAC10 (*32*). We also assessed on-target activity of TYA-018 by measuring Ac-Tubulin in iPSC-CMs (Fig. 4, C to E). The data suggest that TYA-018 is more potent and selective than tubastatin A. We further interrogated TYA-018 in a cell-based assay by measuring acetylated lysine on histone H3 and H4. We did not detect any off-target activity of TYA-018 on nuclear HDACs, indicating high selectivity (Fig. 4E).

We confirmed the selectivity of TYA-018 in a full set of biochemical assays using HDAC1 through HDAC11 (fig. S6A). TYA-018 had more than 2500-fold selectivity compared with other
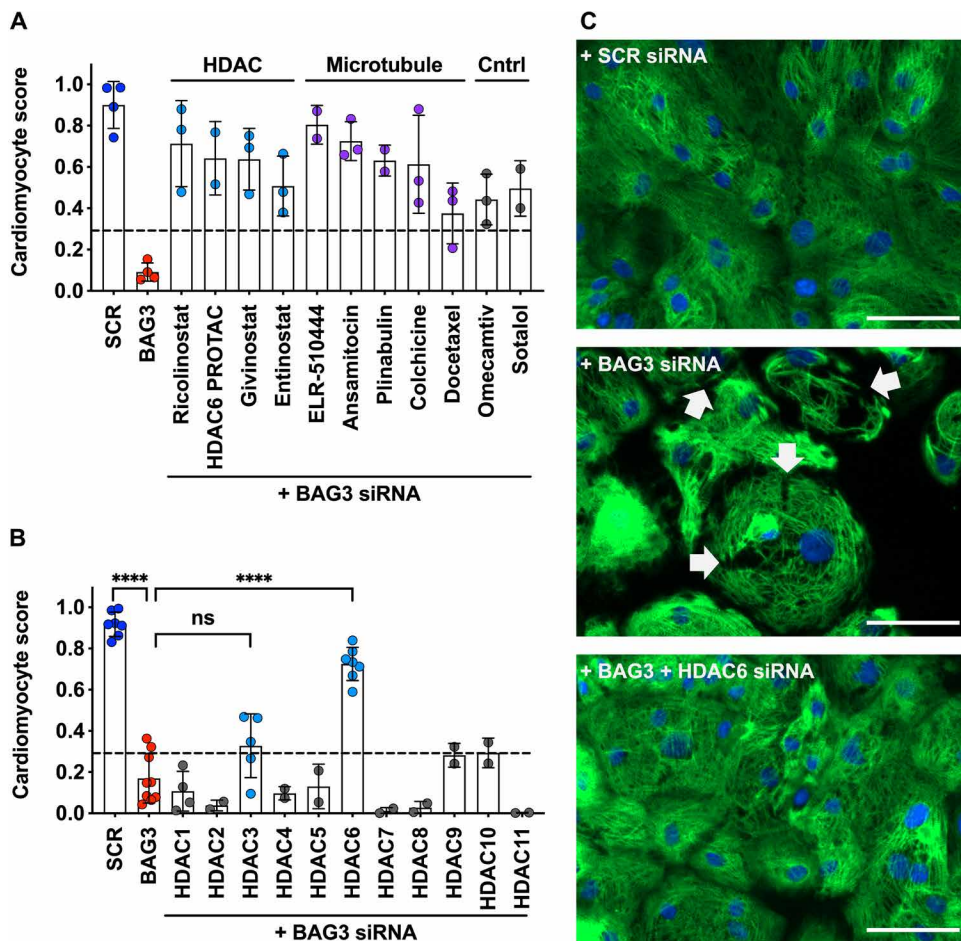
Fig. 3. Target validation studies show inhibiting HDAC6 alone protects against sarcomere damage in BAG3-deficient iPSC-CMs. (**A**) Top compound classes (HDAC inhibitors and microtubule inhibitors) from the library screen and two cardiovascular standard-of-care agents [omecamtiv mecarbil (Omecamtiv) and sotalol] identified from the screen were validated at a 1 μM dose using the cardiomyocyte score. Data from two to four independent biological replicates. *N* = 4 to 16 technical replicates per biological replicate. Cntrl, control. (**B**) Further validation using siRNAs to knock down HDACs in BAG3KD iPSC-CMs using the cardiomyocyte score with the deep learning algorithm. Data from two to four independent biological replicates. *N* = 4 to 16 technical replicates per biological replicate. (**C**) Representative immunostaining of anti-MYBPC3 and Hoechst counterstain in iPSC-CMs treated with SCR, BAG3, or BAG3+HDAC6 siRNA. Arrows indicate sarcomere damage. Scale bar, 50 μm. Data are shown as means ± SD. Multiple comparisons were made using one-way ANOVA. ****$P < 0.0001$.

that the activity of TYA-018 is not associated with transcriptional activation in WT iPSC-CMs (fig. S7, A to C). In addition, treating HDAC6 KO cells with TYA-018 does not increase the intensity of Ac-Tubulin (fig. S7, D and E).

Cardiomyocyte-specific KO of BAG3 in mice leads to heart failure

We used a cardiomyocyte-specific BAG3-KO mouse (BAG3cKO) as a general model of DCM (fig. S8A) (*6*) and to test the efficacy of HDAC6 inhibitors. Although BAG3 loss of function accounts for only ~3% of variant distribution in DCM genes (*16*), we chose this model because BAG3 is a central node in protein quality control for sarcomeric proteins, and it is involved in maintaining myocyte function (*6*, *9*, *20*). In addition, as reported by Fang and colleagues (*6*), this mouse model shows a steady decline in heart function and death because of heart failure. We found that by 5 months old, the mice showed an average ejection fraction of ~30% and a survival rate of ~50% (fig. S8, B and C). We also found that left ventricular internal diameter at diastole (LVIDd), left ventricular internal diameter at systole (LVIDs), and left ventricular mass were significantly greater in BAG3cKO mice versus their WT littermates (*P* < 0.05; fig. S8D). M-mode echocardiography tracings from BAG3cKO mice showed a steady decline in heart function from 1 to 5 months old (fig. S8E). This steady decline in heart function gives an ideal window of opportunity to intervene with a therapeutic small molecule.

Givinostat and tubastatin A prevent progression of heart failure in BAG3cKO mice

To evaluate the translatability of our findings from in vitro screening to an in vivo model, we conducted an efficacy study in BAG3cKO mice using a pan-HDAC inhibitor (givinostat) and HDAC6-selective inhibitor (tubastatin A). Previous literature suggested that pan-HDAC inhibitors provide protection in various heart failure models (*33–35*). First, we used both inhibitors to assess what percentage of efficacy comes from inhibiting only HDAC6 and whether inhibiting other HDACs has additional benefits. Both givinostat and tubastatin A have similar biochemical and cell-based potencies for HDAC6 inhibition (Fig. 4, B and C).

We started administering daily doses of givinostat (30 mg/kg by oral gavage) and tubastatin A (50 mg/kg by intraperitoneal injection) when mice were 1 month old (Fig. 5A). At this age, BAG3cKO mice show significantly lower (~13%, *P* < 0.0001) heart function, as measured by ejection fraction, than WT littermate controls (Fig. 5, B and H).
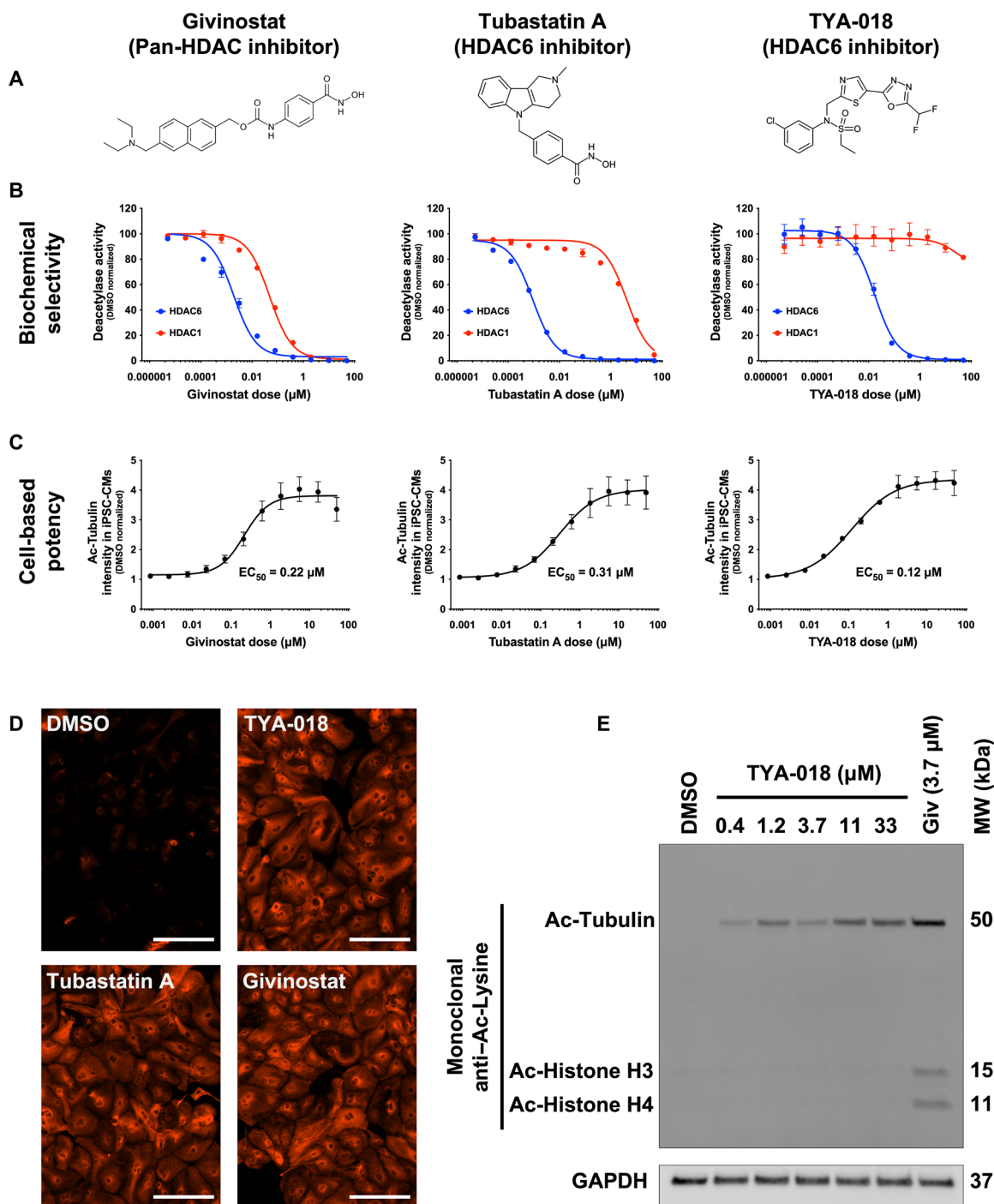
zinc-dependent HDACs (fig. S6B). Using immunostaining for acetylated lysine, we confirmed that TYA-018 does not have off-target HDAC6 activity (fig. S6C). Next, we interrogated cellular toxicity of TYA-018 in human embryonic kidney cells and showed that a lethal dose (LD$_{50}$) is greater than 50 μM (fig. S6D). Last, with a pro-B-type natriuretic peptide (ProBNP) assay, we found that TYA-018 did not dose-dependently increase ProBNP concentration, as seen with givinostat and tubastatin A (fig. S6E).

Next, we performed RNA-seq on WT iPSC-CMs treated with TYA-018, givinostat, and two HDAC6-selective inhibitors (tubastatin A and ricolinostat). Raw RNA-seq data are available on the Gene Expression Omnibus (GEO) database (GSE180248) and provided in table S2. With increasing selectivity, we reduced the number of genes with altered transcript expression in iPSC-CMs. These findings further confirm the high selectivity of TYA-018 for HDAC6, ensuring

Yang *et al.*, *Sci. Transl. Med.* **14**, eabl5654 (2022)   6 July 2022

5 of 15

Fig. 4. TYA-018 is a highly selective HDAC6 inhibitor. (**A**) Chemical structures of givinostat, tubastatin A, and TYA-018. (**B**) Biochemical assays using recombinant human HDAC6 and HDAC1 deacetylase activity showing inhibition curves after treatment with givinostat (pan-HDAC inhibitor), tubastatin A (HDAC6-selective inhibitor), and TYA-018 (HDAC6-selective inhibitor). (**C**) Cell-based assay in iPSC-CMs showing the dose-response curve of tubulin acetylation (Ac-Tubulin) with drug concentrations. EC_{50}, half maximal effective concentration. (**D**) Immunostaining of iPSC-CMs treated with 5.5 μM each drug stained with anti–Ac-Tubulin antibody. Scale bar, 200 μm. MW, molecular weight (**E**) Western blot of iPSC-CMs treated with TYA-018 (HDAC6-specific inhibitor) stained with monoclonal anti–Ac-Lysine. Giv, givinostat (pan-HDAC inhibitor control). Data are shown as means ± SD.

Over the 10-week treatment, daily administration of both givinostat and tubastatin A prevented the progression of heart failure (Fig. 5, B to E and H to K). In addition, LVIDd and LVIDs were significantly reduced in BAG3cKO mice treated with givinostat ($P <$ 0.05 for LVIDd and $P < 0.001$ for LVIDs; Fig. 5, F and G) or tubastatin A ($P < 0.01$ for LVIDd and $P < 0.001$ for LVIDs; Fig. 5, L and M). On the basis of these efficacy studies, inhibiting HDAC6 alone provided cardioprotection against heart failure in BAG3cKO mice. In addition, polypharmacology associated with a pan-HDAC inhibitor did not provide further cardioprotection in these mice.

Tubastatin A protects against heart failure in BAG3E455K mice
To mimic patient-specific mutations, we used a second mouse model containing a human mutation of *BAG3* (BAG3E455K; fig. S9A) (*6*). Mutations in this domain of *BAG3* disrupt the interaction between BAG3 and HSP70, destabilizing the chaperone complex needed to maintain protein quality control and homeostasis in the cell (*6*). Because only HDAC6 inhibition provided sufficient cardioprotection, we began a third efficacy study in BAG3E455K mice. To test whether later interventions could protect against heart failure, we treated these mice with tubastatin A (50 mg/kg by intraperitoneal injection) at 3 months old. After 6 weeks of treatment, tubastatin A provided cardioprotection, including improved ejection fraction (fig. S9, B to G), in BAG3E455K mice. Tubastatin A also reduced the mortality rate due to heart failure in BAG3E455K mice (fig. S9H). Protection against death due to heart failure was more pronounced in male mice (fig. S9I), supporting studies that found that males are more susceptible to BAG3 loss of function (*36*).

TYA-018 selectively inhibits HDAC6, reducing *Nppb* expression and sarcomere damage and preventing heart failure in BAG3cKO mice
We tested the efficacy of the novel, highly selective HDAC6 inhibitor TYA-018 in BAG3cKO mice. In this fourth efficacy study, we treated mice daily with TYA-018 (15 mg/kg by oral gavage) starting at 2 months old (Fig. 6A). Similar to the efficacy studies with givinostat and tubastatin A, TYA-018 conferred cardioprotection in these mice during the 8-week dosing period, as indicated by the increased ejection fraction (Fig. 6, B to E) and significantly reduced LVIDs ($P < 0.05$; Fig. 6, F and G). Because TYA-018 is highly selective for HDAC6 (fig. S6) and structurally distinct from tubastatin A (Fig. 4A), this efficacy study confirms that HDAC6 inhibition exclusively drives the cardioprotection. The cardioprotective effects of TYA-018 were not tested in BAG3E455K mice.

At 4 months old, after 8 weeks of dosing with TYA-018, we collected and processed hearts from mice in the efficacy study. qPCR analysis of brain natriuretic peptide [a cardiac stress heart failure biomarker (*37–39*) encoded by the *Nppb* gene] showed an about threefold increase in BAG3cKO mouse hearts. TYA-018 treatment significantly reduced *Nppb* expression to near WT ($P < 0.001$; Fig. 6H). Heart tissue also showed a slightly increased percentage (1.3%) of trichrome-positive tissue in BAG3cKO mice versus their WT littermates, suggesting that BAG3cKO mice at 4 months old do not have substantial fibrosis in the heart. TYA-018 treatment reduced fibrosis in BAG3cKO mice, albeit not significantly ($P = 0.55$) (Fig. 6I). Heart tissues also showed higher filamin-C (FLNC), phosphatase and tensin homolog–induced kinase 1 (PINK1), and voltage-dependent anion channel 2 (VDAC2) and lower HSPB8 and p62 in BAG3cKO mice versus WT mice (Fig. 6J). In BAG3cKO mice, TYA-018 treatment

partially restored protein expression of FLNC, PINK1, VDAC2, and p62 to amounts similar to WT mice. In addition, alpha-actinin-2 (ACTN2) and hematoxylin and eosin staining show sarcomere damage, reduced content, and myofibril disarray in hearts from BAG3cKO mice versus those from WT mice and BAG3cKO mice treated with TYA-018 (Fig. 6, K and L). TYA-018 treatment significantly reduced the percentage of cardiomyocytes with damaged and reduced sarcomeres in BAG3cKO mice ($P < 0.01$; Fig. 6M).

TYA-018 treatment reduces mitochondrial content, decreases apoptotic nuclei, and increases LC3 puncta in hearts of BAG3cKO mice
Immunohistochemistry with a mitochondrial-specific antibody showed greater mitochondrial content in BAG3cKO mouse hearts (Fig. 7A), suggesting a high energy demand potentially due to increased sarcomere damage and myofibril disarray. In BAG3cKO mice, TYA-018 significantly reduced mitochondrial content to amounts similar to WT mice ($P < 0.05$; Fig. 7, A to E). Using immunohistochemistry, we saw higher fragmented and terminal deoxynucleotidyl transferase–mediated deoxyuridine triphosphate nick end labeling–positive (TUNEL+) nuclei in BAG3cKO mice versus their WT littermates ($P < 0.05$). However, TYA-018 did not reduce fragmented and TUNEL+ nuclei in BAG3cKO mice (Fig. 7, F to H, and fig. S10, A and B). In addition, with immunostaining using microtubule-associated protein light chain 3 (LC3), which regulates autophagosome formation, we observed greater LC3 puncta and a higher percentage of LC3+ areas in hearts from BAG3cKO mice treated with TYA-018 (Fig. 7I). The percentage of LC3+ areas correlated with ejection fraction (Fig. 7J), suggesting that activating autophagy and clearing damaged mitochondria may be part of the cardioprotective mechanism of HDAC6 inhibitors. However, single-agent and co-drug treatment studies in iPSC-CMs did not indicate activation of autophagic flux based on ratios of LC3II/LC3I and p62 (fig. S10, C and D). This result suggests that a more mature cell system may be needed to detect activation of autophagic flux in iPSC-CMs. As part of our mechanistic studies, we tested whether TYA-018 affects acetylation of the antioxidant peroxiredoxin 1 (PRDX1). The acetylation status of PRDX1 did not differ after TYA-018 treatment (fig. S10E).

TYA-018 treatment enriches targets associated with muscle contraction, protein and fatty acid metabolism, and oxidative phosphorylation in BAG3cKO mice
We conducted transcriptomics and proteomics analysis of coding genes in hearts harvested from the three arms (WT+Veh, BAG3cKO+Veh, and BAG3cKO+TYA-018) in the fourth efficacy study. Raw RNA-seq data are available on the GEO database (GSE179656) and provided in table S3. Principal component analysis showed that WT and BAG3cKO mice form two distinct clusters, and the BAG3cKO+TYA-018 mice cluster between WT and BAG3cKO mice (Fig. 8A). This analysis showed a global correction of BAG3cKO+TYA-018 coding genes toward their WT littermates. The RNA-seq data showed an about fourfold increase in *Nppb* expression in BAG3cKO mice versus WT mice at 4 months old. TYA-018 reduced *Nppb* expression in BAG3cKO mice, and *Nppb* expression was anticorrelated ($R < −0.6$) with ejection fraction (Fig. 8B). In BAG3cKO mice treated with TYA-018, the top enriched terms in the biological process category included fatty acid oxidation, respiratory electron transport chain, mitochondrial adenosine triphosphate (ATP) transport, and muscle contraction (fig. S11A). The data showed trending correction of key sarcomere
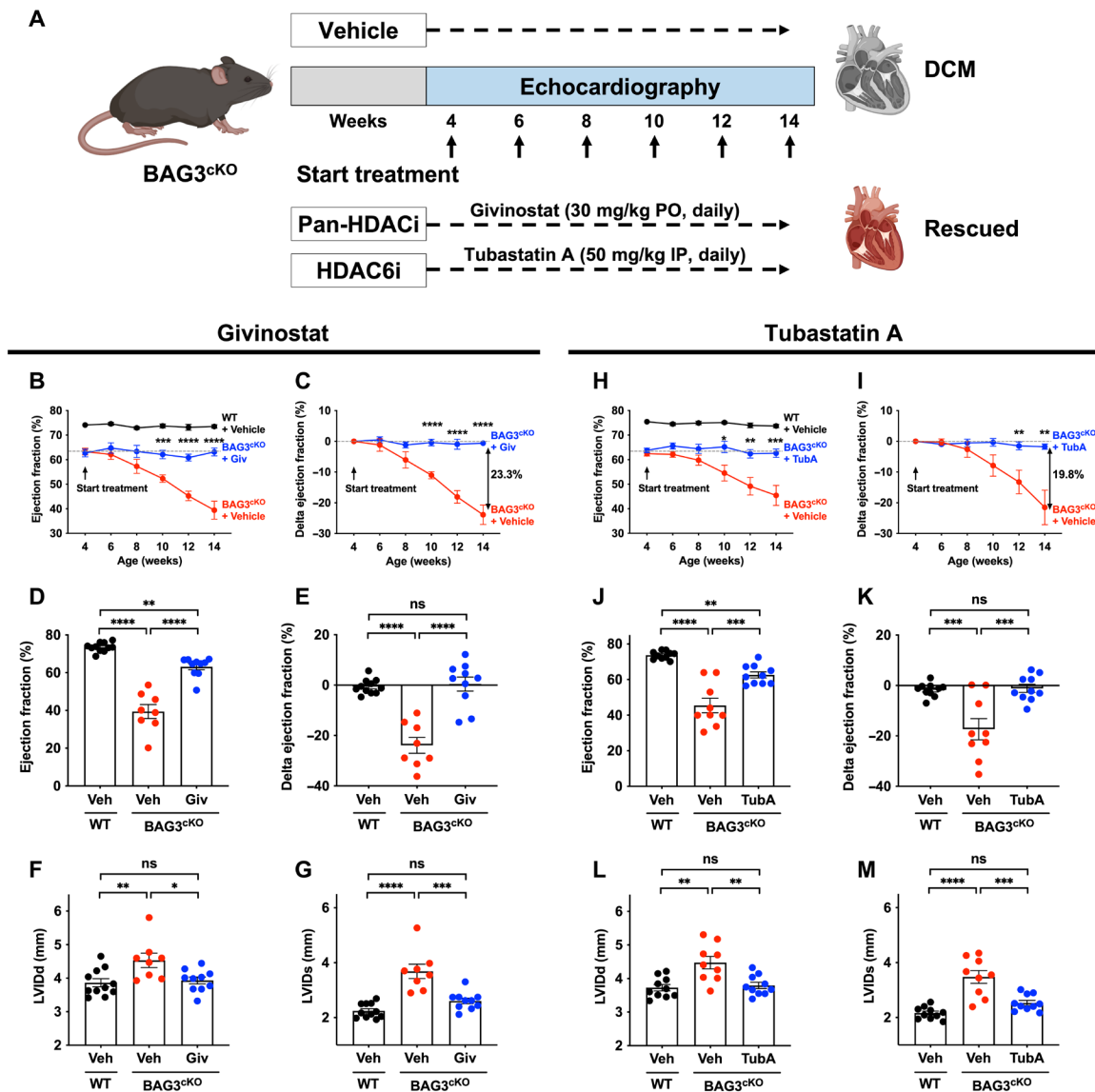
Fig. 5. Givinostat and tubastatin A protect heart function in BAG3^{cKO} mouse. (**A**) Schematic of drug treatments in BAG3^{cKO} mouse model. Daily dosing began in 1-month-old mice. Givinostat (Giv; pan-HDAC inhibitor) was administered daily by oral gavage (PO) at 30 mg/kg. Tubastatin A (TubA; HDAC6-selective inhibitor) was administered daily by intraperitoneal injection (IP) at 50 mg/kg. (**B**) Ejection fraction and (**C**) delta ejection fraction measured from the first day of dosing. (**D** and **E**) Ejection fraction (D) and delta ejection fraction (E) (compared to the predose baseline) at 3.5 months old and after 10 weeks of dosing with givinostat or vehicle in BAG3^{cKO} mice compared to WT. Veh, vehicle. (**F** and **G**) Left ventricular internal diameter at diastole (LVIDd) (F) and systole (LVIDs) (G) in BAG3^{cKO} mice treated with givinostat or vehicle, compared to WT littermates. (**H**) Ejection fraction and (**I**) delta ejection fraction measured from the first day of dosing. (**J** and **K**) Ejection fraction (J) and delta ejection fraction (K) (compared to the predose baseline) at 3.5 months old and after 10 weeks of dosing with tubastatin A or vehicle in BAG3^{cKO} mice compared to WT. (**L** and **M**) LVIDd (L) and LVIDs (M) in BAG3^{cKO} mice tread with tubastatin A or vehicle compared to WT littermates. Data are shown as means ± SEM. Multiple comparisons were made using one-way ANOVA. *$P < 0.05$, **$P < 0.01$, ***$P < 0.001$, and ****$P < 0.0001$.

genes (*Myh7*, *Tnni3*, and *Myl3*) and genes that regulate metabolism and mitochondrial function (*Cyc1*, *Ndufs8*, *Ndufb8*, and *Prkag2*). The data also showed reduced expression of genes associated with inflammation (*Il-1b* and *Nlrp3*) and apoptosis (*Casp1* and *Casp8*) markers (fig. S11B).

Next, we generated a heatmap of genes from the selected enriched Gene Ontology (GO) terms, which showed similar gene expression in WT and BAG3^{cKO} mice treated with TYA-018 (Fig. 8C). We also performed GO enrichment analysis of genes positively correlated ($R > 0.5$) with cardiac function (% ejection fraction) and negatively

correlated ($R < -0.5$) with *Nppb* expression (fig. S11, C and D, and table S4). We also validated a subset of these targets using qPCR (fig. S11E). The genes up-regulated in control and TYA-018–treated mice encode enzymes that regulate different steps of fatty acid β-oxidation, mitochondrial ATP transport, the respiratory electron transport chain, and muscle contraction.

Differential expression analysis using transcriptomics showed up-regulation of transcripts involved in phagosome formation and maturation, the proteasome complex, and oxidative phosphorylation (Fig. 8D). To determine whether these transcriptional changes
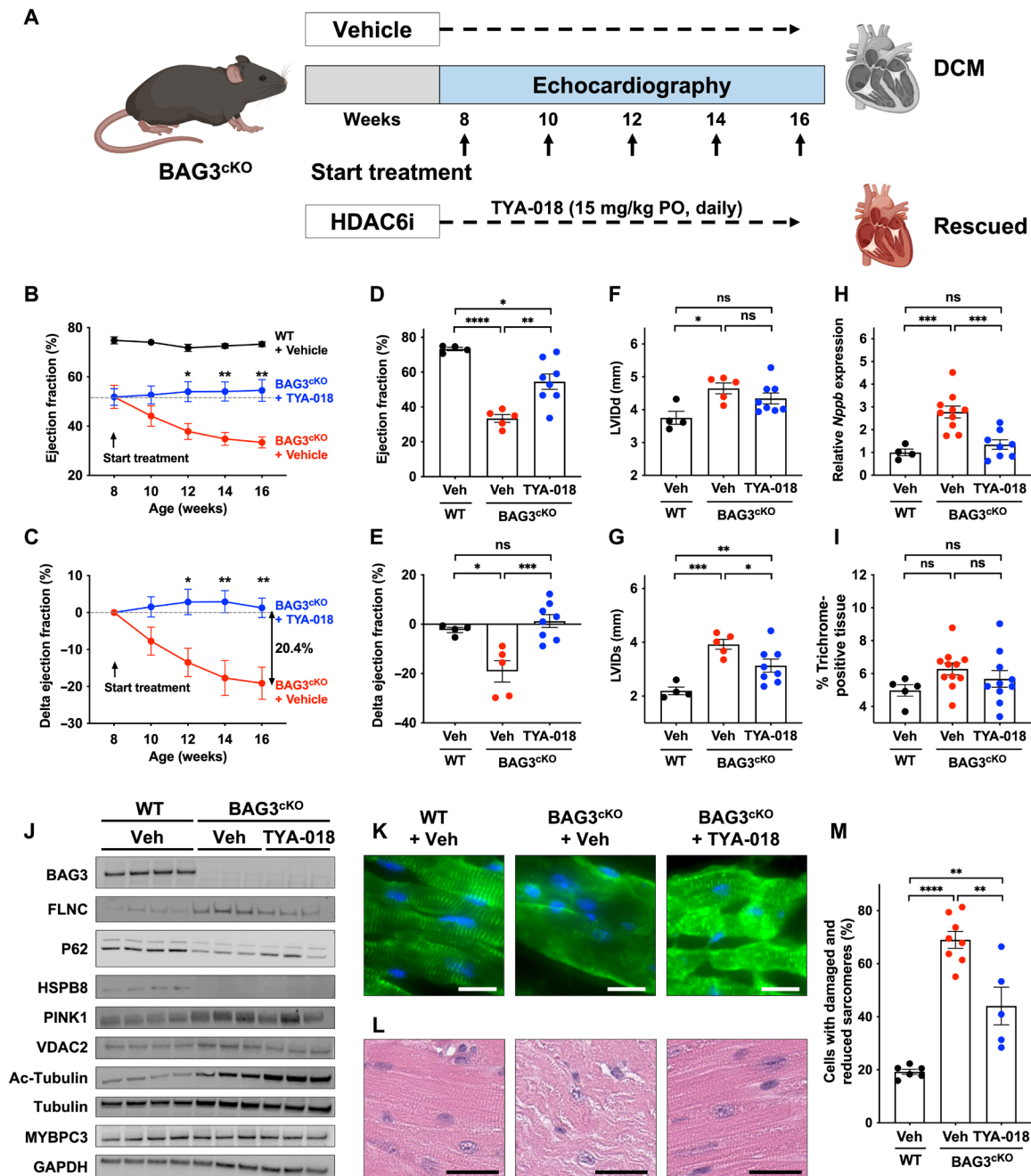
Yang *et al.*, *Sci. Transl. Med.* **14**, eabl5654 (2022)   6 July 2022

8 of 15

Fig. 6. Inhibiting HDAC6 with TYA-018 protects heart function in BAG3cKO mice. (**A**) Schematic of drug treatment in BAG3cKO mouse model. TYA-018 (highly selective HDAC6 inhibitor) was administered daily by oral gavage (PO) at 15 mg/kg starting when mice were 2 months old. (**B**) Ejection faction and (**C**) delta ejection fraction measured from the first day of dosing. (**D** and **E**) Ejection fraction (D) and delta ejection fraction (E) (compared to the predose baseline) at 4 months old and after 8 weeks of dosing with TYA-018 or vehicle in BAG3cKO mice compared to WT. (**F** and **G**) TYA-018 reduced LVIDd (F) and LVIDs (G) in BAG3cKO mice, bringing them closer to that of their WT littermates. (**H**) qPCR analysis showing *Nppb* expression in BAG3cKO mouse hearts compared to WT. (**I**) Percentage of trichrome-positive tissue in BAG3cKO and WT littermate hearts. (**J**) Representative Western blots of heart tissue from BAG3cKO mice and WT. (**K**) Representative ACTN2 staining of sarcomeres in hearts from BAG3cKO mice versus hearts from WT mice. Scale bar, 50 μm. (**L**) Representative hematoxylin and eosin staining of myofibril organization in hearts from BAG3cKO mice versus WT mice. Scale bar, 50 μm. (**M**) Quantification of sarcomere damage and reduced content in mouse hearts. Data are shown as means ± SEM. Multiple comparisons were made using one-way ANOVA. *$P < 0.05$, **$P < 0.01$, ***$P < 0.001$, and ****$P < 0.0001$.

translate to protein changes, we analyzed proteomics in WT, BAG3cKO, and BAG3cKO+TYA-018 mouse hearts using label-free mass spectrometry. To visualize the biomolecule-interaction network, we used GO enrichment analysis with Cytoscape. We found several

pathways commonly altered in BAG3cKO+TYA-018 mouse hearts by both transcriptomics and proteomics. These pathways maintain normal cardiac function, muscle contraction, protein folding, energy metabolism through oxidative phosphorylation, protein
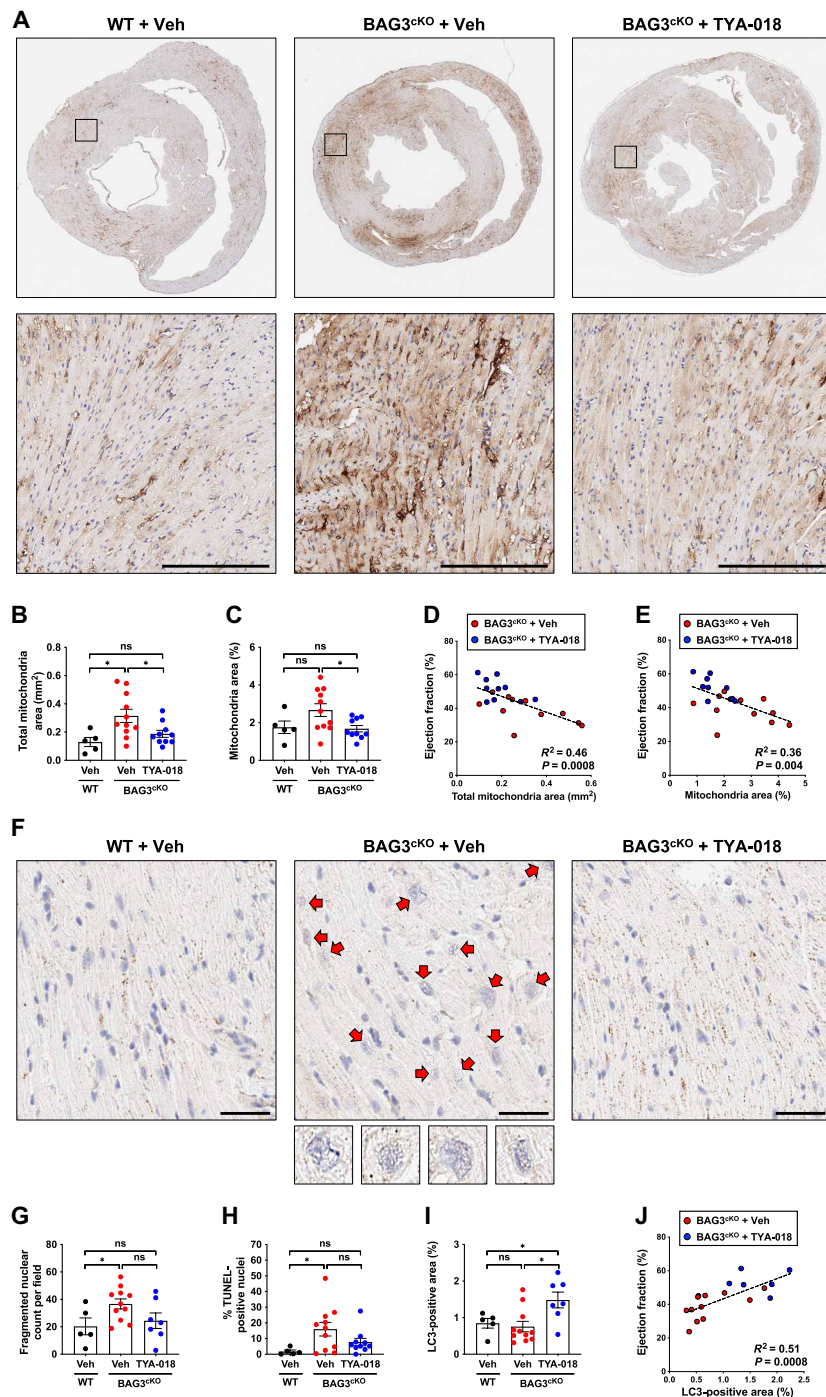
Fig. 7. TYA-018 treatment reduced mitochondrial content, decreased TUNEL-positive apoptotic nuclei, and increased LC3 puncta in hearts of BAG3[cKO] mice. (**A**) Representative immunohistochemistry of mouse hearts with an antibody targeting mitochondrial-specific proteins. Scale bars, 200 μm. (**B** and **C**) Quantification of total mitochondrial area (B) and percentage mitochondrial area (C). (**D** and **E**) Anticorrelation of total mitochondrial area (D) and percentage mitochondrial area (E) with heart function in hearts from BAG3[cKO]+TYA-018 mice. (**F**) Immunohistochemistry of mouse hearts with an LC3 antibody with nuclear stain showing fragmented nuclei. Arrows indicate fragmented nuclei in BAG3[cKO] mouse hearts. Lower boxes show representative enlarged images of the fragmented nuclei. Scale bars, 200 μm. (**G** and **H**) Image quantification of fragmented nuclei (G) and TUNEL-positive nuclei (H) in hearts isolated from BAG3[cKO] mice versus WT mice. (**I**) Quantification of LC3-positive area in BAG3[cKO] hearts versus WT. (**J**) Correlation of LC3-positive area with heart function in the hearts of BAG3[cKO]+TYA-018 mice. Data are shown as means ± SEM. Multiple comparisons were made using one-way ANOVA. *$P < 0.05$.

and fatty acid metabolism, and cytoskeleton and mitochondrial organization (Fig 8E and table S5).

TYA-018 treatment improves mitochondrial membrane potential and function in iPSC-CMs

To test how TYA-018 affects mitochondrial membrane potential and function, we measured tetramethylrhodamine, methyl ester (TMRM) in iPSC-CMs. TMRM accumulates in the membrane of active mitochondria and is commonly used to indicate mitochondrial health (*40*). With TMRM fluorescent staining, we found that iPSC-CMs treated with TYA-018 (1 μM) had significantly greater mitochondrial membrane potential than those treated with dimethyl sulfoxide (DMSO; control; $P < 0.01$; Fig. 8, F and G). In addition, when measuring mitochondrial respiration with the Seahorse Respirometry Mito Stress Test, we found that iPSC-CMs treated with TYA-018 (1 μM) showed no significant difference in basal respiration rate (Fig. 8H). However, iPSC-CMs did show significantly greater reserve respiratory capacity than those treated with DMSO ($P < 0.05$; Fig. 8I). These results suggest that HDAC6 inhibition improves mitochondrial function in iPSC-CMs and augments their capacity to respond to a metabolic demand.
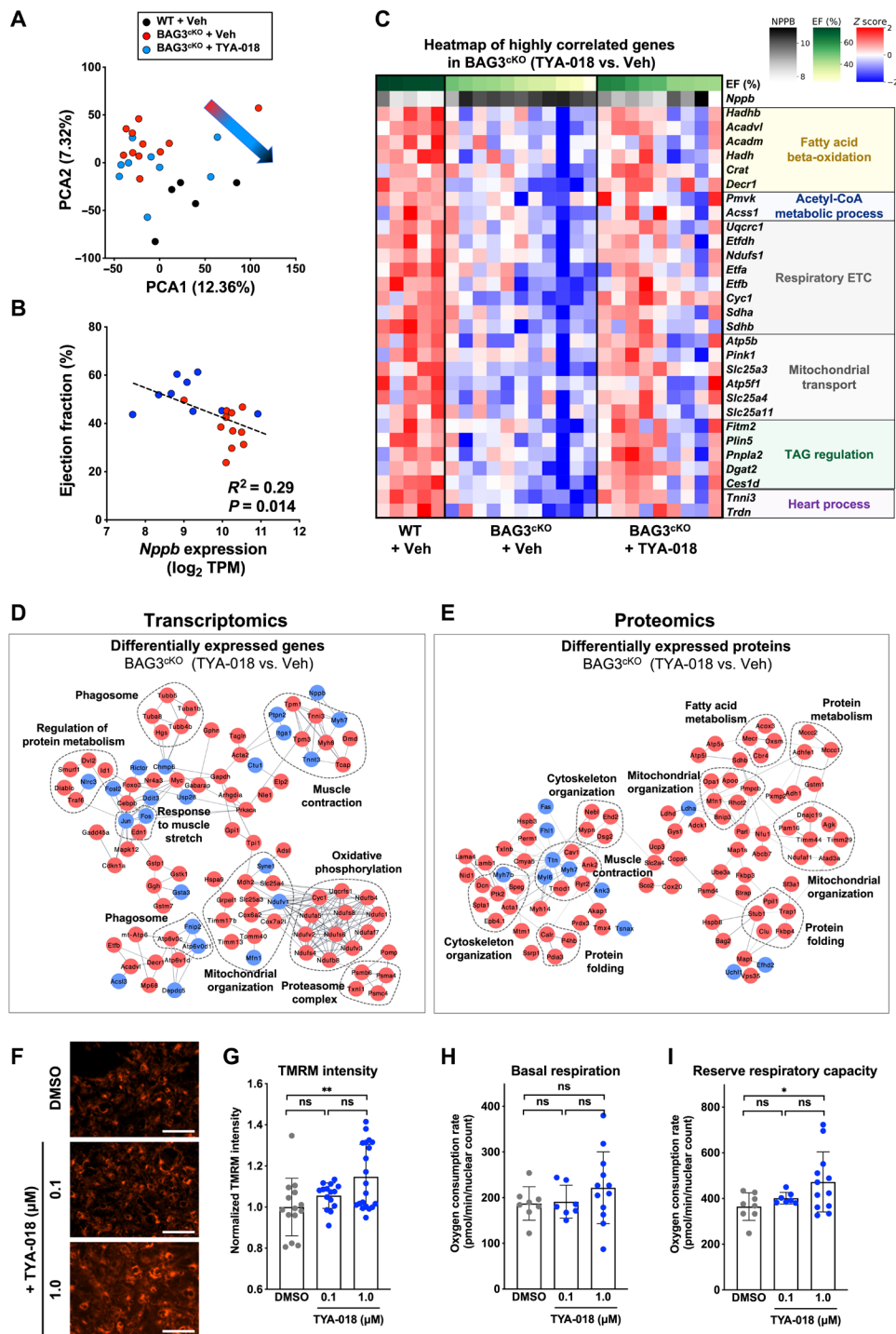
DISCUSSION

In this study, we aimed to identify small-molecule targets that could lead to novel therapeutics for cardiomyopathies, such as BAG3-related DCM. Using high-content screening that combines deep learning with BAG3-deficient iPSC-CMs, we screened 5500 bioactive compounds. We identified HDAC and microtubule inhibitors as two target classes that protect sarcomeres from damage induced by BAG3 knockdown. We also identified heart failure agents [approved by the Food and Drug Administration (FDA) or in late-stage clinical trials] that have shown clinical benefit in heart failure patients (omecamtiv mecarbil, sotalol, and colchicine), supporting the translational relevance of this phenotypic screening strategy. Using siRNAs, we further characterized the polypharmacology associated with HDAC inhibitors. We found that HDAC6 was the only isoform that protects sarcomeres from damage associated with BAG3 loss of function in iPSC-CMs.

We translated these findings to an in vivo setting by treating rodent models of DCM (BAG3[cKO] and BAG3[E455K] mice) with HDAC6 inhibitors. We used a known HDAC6 inhibitor (tubastatin A) and a highly selective HDAC6 inhibitor with a novel zinc-binding domain (TYA-018). Both tubastatin A (>100-fold selectivity over other HDACs) and TYA-018 (>2500-fold selectivity over other HDACs)

Fig. 8. TYA-018 restores dysregulated cardiac and metabolic transcripts in BAG3^{cKO} hearts.
(**A**) Hearts from all three arms of the study were analyzed using RNA-seq. Principal component analysis of genes with quantifiable expression in at least 10% of samples showed a global correction of BAG3^{cKO}+TYA-018 coding genes toward WT mice (arrow). (**B**) Anticorrelation of *Nppb* with heart function in BAG3^{cKO}+TYA-018 mice. (**C**) Heatmap of genes selected from Gene Ontology (GO) terms. The genes up-regulated in BAG3^{cKO}+TYA-018–treated mice encode major enzymes that regulate different steps of fatty acid β-oxidation (*Acadvl*, *Acadm*, *Hadh*, and *Hadhb*), mitochondrial ATP transport (*Atp5b*, *Atp5f1*, *Slc25a3*, and *Slc25a11*), the respiratory electron transport chain (*Ndufs1*, *Etfa*, *Etfb*, *Cyc1*, and *Etfdh*), and muscle contraction (*Tnni3* and *Trdn*). Network visualization of genes (**D**) and proteins (**E**) that are highly differentially expressed in BAG3^{cKO} mice treated with TYA-018 versus vehicle. Red nodes represent up-regulated targets, and blue nodes represent down-regulated targets. Differential expression analysis using transcriptomics showed up-regulation of transcripts involved in phagosome formation and maturation, proteasome complex, and oxidative phosphorylation. Other differentially expressed transcripts were involved in muscle contraction, regulation of protein metabolism, and mitochondrial organization. Differential expression analysis using proteomics data showed up-regulation of targets involved in protein metabolism and folding, cytoskeleton and mitochondrial organization, and fatty acid metabolism. Enriched GO terms of network modules were defined by the functional annotation tool for the search tool for the retrieval of interacting genes/proteins (STRING). The minimum required interaction score was set to 0.4, and the edge thickness indicated the degree of data support. (**F**) Representative fluorescent staining of TMRM, indicative of mitochondrial membrane potential, in iPSC-CMs after exposure to TYA-018 or DMSO control. Scale bars, 200 μm. (**G**) Quantification of average florescent TMRM signal (normalized to DMSO) in iPSC-CMs treated with TYA-018 (1 μM) versus DMSO control. (**H** and **I**) Quantification of (H) basal respiration and (I) reserve respiratory capacity (measured by the oxygen consumption rate) in iPSC-CMs after treatment with TYA-018 (1 μM) versus DMSO control. Data are shown as means ± SD. Multiple comparisons were made using one-way ANOVA. *$P < 0.05$ and **$P < 0.01$.

were efficacious in BAG3^{cKO} mice and protected them from declining heart function compared to vehicle treatment. Tubastatin A also protected BAG3^{E455K} mice against declining heart function and reduced their mortality compared to vehicle control. The cardioprotective effects of TYA-018 were not tested in BAG3^{E455K} mice.

Several pan-HDAC inhibitors have cardioprotective effects in pressure overload, ischemia/reperfusion, and transgenic rodent models.

These inhibitors include suberoylanilide hydroxamic acid (*35*, *41*, *42*), trichostatin A (*33*), and givinostat (*34*, *43*, *44*). Because these inhibitors target multiple isoforms of HDACs, it was difficult to distinguish which HDAC isoform was inhibited to confer cardioprotection. Other researchers found that tubastatin A restored impaired left ventricular ejection fraction mediated by angiotensin II and that HDAC6 KO improved cardiac function in mice treated with

angiotensin II and subjected to transaortic constriction surgery (45). We found that inhibiting HDAC6 alone was cardioprotective in DCM mouse models (BAG3[cKO] and BAG3[E455K]). Treatment with the pan-HDAC inhibitor givinostat in BAG3[cKO] was not more efficacious than an HDAC6-selective inhibitor, supporting that inhibiting HDAC6 alone provides cardioprotection in a DCM model. Inhibiting HDAC6 prevented declining heart function but did not improve heart function above baseline in BAG3[cKO] and BAG3[E455K] mice.

Our study indicates that inhibiting HDAC6 alone does not lead to histone deacetylation nor alter the transcriptional profile in iPSC-CMs. This important finding excludes a mechanism that alters cellular transcriptional programs, which could affect expression of key developmental, regulatory, and ion-channel genes (46–49). HDAC6-selective inhibitors have lower cytotoxicity because of the cytoplasmic location of HDAC6 substrates and reduced effects on nuclear targets and global transcription (50). Our studies also indicate that treating with givinostat (pan-HDAC inhibitor) and ricolinostat (partially selective HDAC6 inhibitor) induces transcriptional changes in iPSC-CMs. Pan-HDAC inhibitors acetylate histones and transcription factors, leading to pleiotropic transcriptional changes that affect cellular functions, such as cell growth, apoptosis, and differentiation (47). In addition, pan-HDAC inhibitors can be highly cytotoxic (51), as most pan-HDAC inhibitors were developed for cancer therapeutics (47, 52). Therefore, a highly selective HDAC6 inhibitor may enable safe and efficacious inhibition of HDAC6 as a therapeutic target for DCM.

Although more translational work is needed to investigate the cardioprotective effects of HDAC6-specific inhibitors in other DCM and large animal models of heart failure, our data support that HDAC6 inhibitors may be promising drug candidates for treating cardiomyopathies. In addition, future studies may be needed to assess whether a combined treatment of an HDAC6 inhibitor with a standard of care (53–55) or gene therapy (20, 56) may synergistically improve heart function in a heart failure model.

Tubulin is a known substrate for HDAC6, and Ac-Tubulin is a posttranslational modification used as a pharmacodynamic marker of HDAC6 activity (27). Long-lived microtubules in the heart undergo frequent buckling because of compressive loads in the heart, and pathogenic modifications and remodeling on tubulin stiffens myocytes and reduces compliance. In myocytes, microtubules are anchored at the Z-disk via desmin (57). Thus, with buckling, microtubules exert force back on the Z-disk, causing long-term mechanical damage at the Z-disk (57, 58). Ac-Tubulin protects microtubules against this mechanical damage (59), implicating that HDAC6 inhibition may directly stabilize and protect microtubules against damage, improve myocyte compliance, and protect the Z-disk. Because sarcomere damage, myofibril disarray, and impaired sarcomere turnover are hallmarks of DCM (1, 16, 20), our study supports that inhibiting HDAC6 provides protection at the sarcomere level in DCM.

Our integrated RNA-seq and proteomics data revealed that HDAC6 inhibition enhanced cardiac energetics. Specifically, our data showed that TYA-018 increased expression of targets associated with fatty acid and protein metabolism, as well as oxidative phosphorylation. These mechanisms could underlie the improved cardiac function in BAG3[cKO] mice treated with TYA-018.

We also found that HDAC6 inhibition enhanced mitochondrial membrane potential and reserve respiratory capacity, supporting our integrated omics data and indicating greater ATP production capacity in human iPSC-CMs. Although more work is needed to fully understand the mechanism underlying the enhanced cardiac energetics and reduced sarcomere damage, one possible mechanism may involve activation of autophagic flux through chaperone-assisted selective autophagy (20). In addition, studies have shown that HDAC6 inhibition signals recruitment of the microtubule-associated protein LC3 that assembles autophagosomes and transports damaged and misfolded proteins (7, 60) and mitochondria (61, 62). In cardiomyopathies, in which protein quality control pathways are impaired, activation of autophagic flux may lead to clearance of damaged mitochondria and misfolded proteins (60, 61, 63).

In summary, our results demonstrate the power of combining iPSC-CMs with phenotypic screening and deep learning to identify therapeutic targets for heart disease. With this approach, we identified HDAC6 as a target in DCM and showed that its inhibition prevented declining heart function in BAG3[cKO] mice. Although future work will need to assess the safety and efficacy of HDAC6 inhibitors in larger animal models and patient populations with cardiomyopathies, HDAC6 inhibitors may be promising candidates for treating cardiomyopathies and other forms of heart failure.

MATERIALS AND METHODS
Study design
The objective of this study was to identify cardioprotective targets using high-content screening and human iPSC-derived cardiomyocytes. The DMSO (5,5-dimethyloxazolidine-2,4-dione) concentration was controlled in all studies. The number of biological and technical replicates (N) per experiment is noted in each figure legend. Mice were randomized before being assigned to either vehicle or treatment groups. At least six mice were assigned for each group. An individual blinded to the genotype and treatment performed echocardiography and another individual analyzed the data. No outliers were removed from the data.

iPSC-CM culture for high-content screening
iCell Cardiomyocytes[2] were thawed according to the manufacturer's instructions (FUJIFILM Cellular Dynamics) directly onto Matrigel-coated 384-well plates at a density of 20,000 cells per well. The next day, the medium was switched to CDI maintenance media (FUJIFILM Cellular Dynamics) for 6 days before screening.

siRNA knockdown
To knock down endogenous expression, iPSC-CMs were transfected with FlexiTube GeneSolution siRNAs (QIAGEN) at a final concentration of 5 nM using Lipofectamine RNAiMAX (Thermo Fisher Scientific) in RPMI+B27 media (Thermo Fisher Scientific). When not specified, a siRNA pool consisting of four independent siRNAs was used. Forty-eight hours after transfection, medium was removed and replaced with fresh CDI media.

qPCR analysis
Real-time qPCR was performed using the TaqMan universal PCR master mix (Thermo Fisher Scientific) with the TaqMan probes listed in table S6. Additional details about this method are provided in Supplementary Methods.

Compound library screening
A library containing 5500 bioactive compounds consisting of FDA-approved drugs, tool compounds, and preclinical drug candidates

was sourced from Selleck Chemicals and TargetMol. After thawing, iPSC-CMs recovered for 6 days in CDI media (FUJIFILM Cellular Dynamics). Then, BAG3 siRNAs were added to the cells (day 0) to induce sarcomere damage. Two days later (day 2), medium was removed and replaced with fresh CDI media. Four days later (day 6), the compound library was added at 1.0 μM in RPMI+B27 media (Thermo Fisher Scientific). After 4 days with the compound library (day 10), cells were fixed in 4% paraformaldehyde for 15 min, stained with MYBPC3 antibody (table S7), and imaged.

Construction of deep learning models and neural network architecture

Deep learning artificial intelligence models were built using the PhenoLearn platform (www.PhenoLearn.com) as described (*21*). We used PyTorch as the framework for the deep learning library and ResNet50 architecture, a 50-layer-deep convolutional neural network. A two-class deep learning model was developed by inputting about 1300 images from either SCR- or BAG3-siRNA–treated conditions. Each input image was divided into 12-square sub-images with sizes ranging from 224 × 224 to 300 × 300 pixels (*64*). We used 80% of the images to construct the neural network and the remaining 20% to validate the deep learning model. For each training, the final neural network was selected from the epoch with the highest validation accuracy. *Z*-factor was calculated using the following formula

$$Z\text{–factor} \;=\; 1 - \frac{3(\sigma_p - \sigma_n)}{|\mu_p - \mu_n|}$$

Animal studies

Animal studies were performed according to Tenaya Therapeutics' animal use guidelines. The animal protocols were approved by the Institutional Animal Care and Use Committee and accredited by the Association for Assessment and Accreditation of Laboratory Animal Care (IACUC number: 2020.007).

Mouse models

BAG3-floxed (BAG3$^{fl/fl}$) mice and BAG3$^{E455K/+}$ (equivalent to the mouse E460K) knock-in mice were obtained from J. Chen's laboratory (University of California San Diego School of Medicine) (*6*). To generate BAG3 cardiomyocyte–specific KO mice, BAG3$^{fl/fl}$ mice were crossed with α-myosin heavy chain–transgenic (αMHC-Cre) mice (strain code: 011038; the Jackson Laboratory). To generated cardiac-specific BAG3$^{E455K-cMUT}$ (αMHC-Cre; BAG$^{fl/E455K}$) mice, BAG3$^{E455K/+}$ mice were crossed with BAG3^{cKO} (αMHC-Cre; BAG3$^{fl/fl}$) mice. Littermate BAG3$^{fl/+}$ αMHC-Cre–negative mice were used as controls. Both male and female mice older than 2 months were used in the study.

Statistical analysis

The number of technical and biological replicates and animals for each experiment are indicated in the figure legends. Statistical analyses were performed using Prism 9. Student's *t* test was used to analyze two unpaired groups and one-way analysis of variance (ANOVA) with Tukey post hoc test was used to compare more than two groups. Significant differences were defined as $P < 0.05$. Error bars in all biochemical and cell-based assays indicate SD. Error bars in all in vivo studies represent SEM. The number of samples and subject-level data are listed in data file S1.

SUPPLEMENTARY MATERIALS

REFERENCES AND NOTES

1. E. M. McNally, J. R. Golbus, M. J. Puckelwartz, Genetic mutations and mechanisms in dilated cardiomyopathy. *J. Clin. Invest.* **123**, 19–26 (2013).
2. E. Villard, C. Perret, F. Gary, C. Proust, G. Dilanian, C. Hengstenberg, V. Ruppert, E. Arbustini, T. Wichter, M. Germain, O. Dubourg, L. Tavazzi, M.-C. Aumont, P. DeGroote, L. Fauchier, J.-N. Trochu, P. Gibelin, J.-F. Aupetit, K. Stark, J. Erdmann, R. Hetzer, A. M. Roberts, P. J. R. Barton, V. Regitz-Zagrosek, U. Aslam, L. Duboscq-Bidot, M. Meyborg, B. Maisch, H. Madeira, A. Waldenström, E. Galve, J. G. Cleland, R. Dorent, G. Roizes, T. Zeller, S. Blankenberg, A. H. Goodall, S. Cook, D. A. Tregouet, L. Tiret, R. Isnard, M. Komajda, P. Charron, F. Cambien, A genome-wide association study identifies two loci associated with heart failure due to dilated cardiomyopathy. *Eur. Heart J.* **32**, 1065–1076 (2011).
3. M. J. Everly, Cardiac transplantation in the United States: An analysis of the UNOS registry. *Clin. Transpl.* , 35–43 (2008).
4. J. G. F. Cleland, A. R. Lyon, T. McDonagh, J. J. V. McMurray, The year in cardiology: Heart failure. *Eur. Heart J.* **41**, 1232–1248 (2020).
5. G. Tarone, M. Brancaccio, Keep your heart in shape: Molecular chaperone networks for treating heart disease. *Cardiovasc. Res.* **102**, 346–361 (2014).
6. X. Fang, J. Bogomolovas, T. Wu, W. Zhang, C. Liu, J. Veevers, M. J. Stroud, Z. Zhang, X. Ma, Y. Mu, D.-H. Lao, N. D. Dalton, Y. Gu, C. Wang, M. Wang, Y. Liang, S. Lange, K. Ouyang, K. L. Peterson, S. M. Evans, J. Chen, Loss-of-function mutations in co-chaperone BAG3 destabilize small HSPs and cause cardiomyopathy. *J. Clin. Invest.* **127**, 3189–3200 (2017).
7. E. Stürner, C. Behl, The role of the multifunctional BAG3 protein in cellular protein quality control and in disease. *Front. Mol. Neurosci.* **10**, 177 (2017).
8. S. Franceschelli, A. Rosati, R. Lerose, S. De Nicola, M. C. Turco, M. Pascale, Bag3 gene expression is regulated by heat shock factor 1. *J. Cell. Physiol.* **215**, 575–577 (2008).
9. L. M. Judge, J. A. Perez-Bermejo, A. Truong, A. J. S. Ribeiro, J. C. Yoo, C. L. Jensen, M. A. Mandegar, N. Huebsch, R. M. Kaake, P.-L. So, D. Srivastava, B. L. Pruitt, N. J. Krogan, B. R. Conklin, A BAG3 chaperone complex maintains cardiomyocyte function during proteotoxic stress. *JCI Insight* **2**, e94623 (2017).
10. J. N. Rauch, E. Tse, R. Freilich, S.-A. Mok, L. N. Makley, D. R. Southworth, J. E. Gestwicki, BAG3 is a modular, scaffolding protein that physically links heat shock protein 70 (Hsp70) to the small heat shock proteins. *J. Mol. Biol.* **429**, 128–141 (2017).
11. S. Carra, S. J. Seguin, H. Lambert, J. Landry, HspB8 chaperone activity toward poly(Q)-containing proteins depends on its association with Bag3, a stimulator of macroautophagy. *J. Biol. Chem.* **283**, 1437–1444 (2008).
12. M. Fuchs, D. J. Poirier, S. J. Seguin, H. Lambert, S. Carra, S. J. Charette, J. Landry, Identification of the key structural motifs involved in HspB8/HspB6-Bag3 interaction. *Biochem. J.* **425**, 245–255 (2009).
13. S. Homma, M. Iwasaki, G. D. Shelton, E. Engvall, J. C. Reed, S. Takayama, BAG3 Deficiency results in fulminant myopathy and early lethality. *Am. J. Pathol.* **169**, 761–773 (2006).
14. V. D. Myers, G. S. Gerhard, D. M. McNamara, D. Tomar, M. Madesh, S. Kaniper, F. V. Ramsey, S. G. Fisher, R. G. Ingersoll, L. Kasch-Semenza, J. Wang, K. Hanley-Yanez, B. Lemster, J. A. Schwisow, A. V. Ambardekar, S. H. Degann, M. R. Bristow, R. Sheppard, J. D. Alexis, D. G. Tilley, C. D. Kontos, J. M. McClung, A. L. Taylor, C. W. Yancy, K. Khalili, J. G. Seidman, C. E. Seidman, C. F. McTiernan, J. Y. Cheung, A. M. Feldman, Association of variants in BAG3 with cardiomyopathy outcomes in African American individuals. *JAMA Cardiol.* **3**, 929–938 (2018).
15. N. Chami, R. Tadros, F. Lemarbre, K. S. Lo, M. Beaudoin, L. Robb, D. Labuda, J.-C. Tardif, N. Racine, M. Talajic, G. Lettre, Nonsense mutations in BAG3 are associated with early-onset dilated cardiomyopathy in French Canadians. *Can. J. Cardiol.* **30**, 1655–1661 (2014).
16. J. Haas, K. S. Frese, B. Peil, W. Kloos, A. Keller, R. Nietsch, Z. Feng, S. Müller, E. Kayvanpour, B. Vogel, F. Sedaghat-Hamedani, W.-K. Lim, X. Zhao, D. Fradkin, D. Köhler, S. Fischer, J. Franke, S. Marquart, I. Barb, D. T. Li, A. Amr, P. Ehlermann, D. Mereles, T. Weis, S. Hassel, A. Kremer, V. King, E. Wirsz, R. Isnard, M. Komajda, A. Serio, M. Grasso, P. Syrris, E. Wicks, V. Plagnol, L. Lopes, T. Gadgaard, H. Eiskjær, M. Jørgensen, D. Garcia-Giustiniani, M. Ortiz-Genga, M. G. Crespo-Leiro, R. H. L. D. Deprez, I. Christiaans, I. A. van Rijsingen, A. A. Wilde, A. Waldenstrom, M. Bolognesi, R. Bellazzi, S. Mörner, J. L. Bermejo, L. Monserrat, E. Villard, J. Mogensen, Y. M. Pinto, P. Charron, P. Elliott, E. Arbustini, H. A. Katus, B. Meder, Atlas of the clinical genetics of human dilated cardiomyopathy. *Eur. Heart J.* **36**, 1123–1135a (2015).

17. N. Norton, D. Li, M. J. Rieder, J. D. Siegfried, E. Rampersaud, S. Züchner, S. Mangos, J. Gonzalez-Quintana, L. Wang, S. McGee, J. Reiser, E. Martin, D. A. Nickerson, R. E. Hershberger, Genome-wide studies of copy number variation and exome sequencing identify rare variants in BAG3 as a cause of dilated cardiomyopathy. *Am. J. Hum. Genet.* **88**, 273–282 (2011).

18. A. A. Ruparelia, V. Oorschot, R. Vaz, G. Ramm, R. J. Bryson-Richardson, Zebrafish models of BAG3 myofibrillar myopathy suggest a toxic gain of function leading to BAG3 insufficiency. *Acta Neuropathol.* **128**, 821–833 (2014).

19. A. M. Feldman, R. L. Begay, T. Knezevic, V. D. Myers, D. B. Slavov, W. Zhu, K. Gowan, S. L. Graw, K. L. Jones, D. G. Tilley, R. C. Coleman, P. Walinsky, J. Y. Cheung, L. Mestroni, K. Khalili, M. R. G. Taylor, Decreased levels of BAG3 in a family with a rare variant and in idiopathic dilated cardiomyopathy. *J. Cell. Physiol.* **229**, 1697–1702 (2014).

20. T. G. Martin, V. D. Myers, P. Dubey, S. Dubey, E. Perez, C. S. Moravec, M. S. Willis, A. M. Feldman, J. A. Kirk, Cardiomyocyte contractile impairment in heart failure results from reduced BAG3-mediated sarcomeric protein turnover. *Nat. Commun.* **12**, 2942 (2021).

21. F. Grafton, J. Ho, S. Ranjbarvaziri, F. Farshidfar, A. Budan, S. Steltzer, M. Maddah, K. E. Loewke, K. Green, S. Patel, T. Hoey, M. A. Mandegar, Deep learning detects cardiotoxicity in a high-content screen with induced pluripotent stem cell-derived cardiomyocytes. *eLife* **10**, e68714 (2021).

22. M. Gamerdinger, A. M. Kaya, U. Wolfrum, A. M. Clement, C. Behl, BAG3 mediates chaperone-based aggresome-targeting and selective autophagy of misfolded proteins. *EMBO Rep.* **12**, 149–156 (2011).

23. Z. Ma, N. Huebsch, S. Koo, M. A. Mandegar, B. Siemons, S. Boggess, B. R. Conklin, C. P. Grigoropoulos, K. E. Healy, Contractile deficits in engineered cardiac microtissues as a result of MYBPC3 deficiency and mechanical overload. *Nat. Biomed. Eng.* **2**, 955–967 (2018).

24. A. Heidersbach, C. Saxby, K. Carver-Moore, Y. Huang, Y.-S. Ang, P. J. de Jong, K. N. Ivey, D. Srivastava, microRNA-1 regulates sarcomere formation and suppresses smooth muscle gene expression in the mammalian heart. *eLife* **2**, e01323 (2013).

25. Y. LeCun, Y. Bengio, G. Hinton, Deep learning. *Nature* **521**, 436–444 (2015).

26. M. Haberland, R. L. Montgomery, E. N. Olson, The many roles of histone deacetylases in development and physiology: Implications for disease and therapy. *Nat. Rev. Genet.* **10**, 32–42 (2009).

27. C. Hubbert, A. Guardiola, R. Shao, Y. Kawaguchi, A. Ito, A. Nixon, M. Yoshida, X.-F. Wang, T.-P. Yao, HDAC6 is a microtubule-associated deacetylase. *Nature* **417**, 455–458 (2002).

28. P. Joshi, T. M. Greco, A. J. Guise, Y. Luo, F. Yu, A. I. Nesvizhskii, I. M. Cristea, The functional interactome landscape of the human histone deacetylase family. *Mol. Syst. Biol.* **9**, 672 (2013).

29. A. Friedrich, A.-S. Assmann, L. Schumacher, J. V. Stuijvenberg, M. U. Kassack, W. A. Schulz, W. P. Roos, F. K. Hansen, M. Pflieger, T. Kurz, G. Fritz, In vitro assessment of the genotoxic hazard of novel hydroxamic acid- and benzamide-type histone deacetylase inhibitors (HDACi). *Int. J. Mol. Sci.* **21**, 4747 (2020).

30. K. V. Butler, J. Kalin, C. Brochier, G. Vistoli, B. Langley, A. P. Kozikowski, Rational design and simple chemistry yield a superior, neuroprotective HDAC6 inhibitor, tubastatin A. *J. Am. Chem. Soc.* **132**, 10842–10846 (2010).

31. L. Santo, T. Hideshima, A. L. Kung, J.-C. Tseng, D. Tamang, M. Yang, M. Jarpe, J. H. van Duzer, R. Mazitschek, W. C. Ogier, D. Cirstea, S. Rodig, H. Eda, T. Scullen, M. Canavese, J. Bradner, K. C. Anderson, S. S. Jones, N. Raje, Preclinical activity, pharmacodynamic, and pharmacokinetic properties of a selective HDAC6 inhibitor, ACY-1215, in combination with bortezomib in multiple myeloma. *Blood* **119**, 2579–2589 (2012).

32. M. Géraldy, M. Morgen, P. Sehr, R. R. Steimbach, D. Moi, J. Ridinger, I. Oehme, O. Witt, M. Malz, M. S. Nogueira, O. Koch, N. Gunkel, A. K. Miller, Selective inhibition of histone deacetylase 10: Hydrogen bonding to the gatekeeper residue is implicated. *J. Med. Chem.* **62**, 4426–4443 (2019).

33. D. J. Cao, Z. V. Wang, P. K. Battiprolu, N. Jiang, C. R. Morales, Y. Kong, B. A. Rothermel, T. G. Gillette, J. A. Hill, Histone deacetylase (HDAC) inhibitors attenuate cardiac hypertrophy by suppressing autophagy. *Proc. Natl. Acad. Sci. U.S.A.* **108**, 4123–4128 (2011).

34. M. Y. Jeong, Y. H. Lin, S. A. Wennersten, K. M. Demos-Davies, M. A. Cavasin, J. H. Mahaffey, V. Monzani, C. Saripalli, P. Mascagni, T. B. Reece, A. V. Ambardekar, H. L. Granzier, C. A. Dinarello, T. A. McKinsey, Histone deacetylase activity governs diastolic dysfunction through a nongenomic mechanism. *Sci. Transl. Med.* **10**, eaao0144 (2018).

35. M. Xie, Y. Kong, W. Tan, H. May, P. K. Battiprolu, Z. Pedrozo, Z. V. Wang, C. Morales, X. Luo, G. Cho, N. Jiang, M. E. Jessen, J. J. Warner, S. Lavandero, T. G. Gillette, A. T. Turer, J. A. Hill, Histone deacetylase inhibition blunts ischemia/reperfusion injury by inducing cardiomyocyte autophagy. *Circulation* **129**, 1139–1151 (2014).

36. F. Domínguez, S. Cuenca, Z. Bilińska, R. Toro, E. Villard, R. Barriales-Villa, J. P. Ochoa, F. Asselbergs, A. Sammani, M. Franaszczyk, M. Akhtar, M. J. Coronado-Albi, D. Rangel-Sousa, J. F. Rodriguez-Palomares, J. Jiménez-Jáimez, J. M. Garcia-Pinilla, T. Ripoll-Vera,

M. V. Mogollón-Jiménez, A. Fontalba-Romero, D. Garcia-Medina, J. Palomino-Doza, D. de Gonzalo-Calvo, M. Cicerchia, J. Salazar-Mendiguchia, C. Salas, S. Pankuweit, T. M. Hey, J. Mogensen, P. J. Barton, P. Charron, P. Elliott, P. Garcia-Pavia; European Genetic Cardiomyopathies Initiative Investigators, Dilated cardiomyopathy due to BLC2-associated athanogene 3 (BAG3) mutations. *J. Am. Coll. Cardiol.* **72**, 2471–2481 (2018).

37. M. Bay, V. Kirk, J. Parner, C. Hassager, H. Nielsen, K. Krogsgaard, J. Trawinski, S. Boesgaard, J. Aldershvile, NT-proBNP: A new diagnostic screening tool to differentiate between patients with normal and reduced left ventricular systolic function. *Heart* **89**, 150–154 (2003).

38. J. Doust, R. Lehman, P. Glasziou, The role of BNP testing in heart failure. *Am. Fam. Physician* **74**, 1893–1898 (2006).

39. J. L. Januzzi, C. A. Camargo, S. Anwaruddin, A. L. Baggish, A. A. Chen, D. G. Krauser, R. Tung, R. Cameron, J. T. Nagurney, C. U. Chae, D. M. Lloyd-Jones, D. F. Brown, S. Foran-Melanson, P. M. Sluss, E. Lee-Lewandrowski, K. B. Lewandrowski, The N-terminal Pro-BNP investigation of dyspnea in the emergency department (PRIDE) study. *Am. J. Cardiol.* **95**, 948–954 (2005).

40. S. Ranjbarvaziri, K. B. Kooiker, M. Ellenberger, G. Fajardo, M. Zhao, A. S. Vander Roest, R. A. Woldeyes, T. T. Koyano, R. Fong, N. Ma, L. Tian, G. M. Traber, F. Chan, J. Perrino, S. Reddy, W. Chiu, J. C. Wu, J. Y. Woo, K. M. Ruppel, J. A. Spudich, M. P. Snyder, K. Contrepois, D. Bernstein, Altered cardiac energetics and mitochondrial dysfunction in hypertrophic cardiomyopathy. *Circulation* **144**, 1714–1731 (2021).

41. S. Nagata, T. Marunouchi, K. Tanonaka, Histone deacetylase inhibitor SAHA treatment prevents the development of heart failure after myocardial infarction via an induction of heat-shock proteins in rats. *Biol. Pharm. Bull.* **42**, 453–461 (2019).

42. M. Wallner, D. M. Eaton, R. M. Berretta, M. Liesinger, M. Schittmayer, J. Gindlhuber, J. Wu, M. Y. Jeong, Y. H. Lin, G. Borghetti, S. T. Baker, H. Zhao, J. Pfleger, S. Blass, P. P. Rainer, D. von Lewinski, H. Bugger, G. Mohsin, W. F. Graier, A. Zirlik, T. A. McKinsey, R. Birner-Gruenberger, M. R. Wolfson, S. R. Houser, HDAC inhibition improves cardiopulmonary function in a feline model of diastolic dysfunction. *Sci. Transl. Med.* **12**, eaay7205 (2020).

43. F. Leoni, G. Fossati, E. C. Lewis, J.-K. Lee, G. Porro, P. Pagani, D. Modena, M. L. Moras, P. Pozzi, L. L. Reznikov, B. Siegmund, G. Fantuzzi, C. A. Dinarello, P. Mascagni, The histone deacetylase inhibitor ITF2357 reduces production of pro-inflammatory cytokines in vitro and systemic inflammation in vivo. *Mol. Med. Camb. Mass* **11**, 1–15 (2005).

44. M. Milan, V. Pace, F. Maiullari, M. Chirivì, D. Baci, S. Maiullari, L. Madaro, S. Maccari, T. Stati, G. Marano, G. Frati, P. L. Puri, E. De Falco, C. Bearzi, R. Rizzi, Givinostat reduces adverse cardiac remodeling through regulating fibroblasts activation. *Cell Death Dis.* **9**, 108 (2018).

45. K. M. Demos-Davies, B. S. Ferguson, M. A. Cavasin, J. H. Mahaffey, S. M. Williams, J. I. Spiltoir, K. B. Schuetze, T. R. Horn, B. Chen, C. Ferrara, B. Scellini, N. Piroddi, C. Tesi, C. Poggesi, M. Y. Jeong, T. A. McKinsey, HDAC6 contributes to pathological responses of heart and skeletal muscle to chronic angiotensin-II signaling. *Am. J. Physiol.-Heart Circ. Physiol.* **307**, H252–H258 (2014).

46. P. Gallinari, S. D. Marco, P. Jones, M. Pallaoro, C. Steinkühler, HDACs, histone deacetylation and gene transcription: From molecular biology to cancer therapeutics. *Cell Res.* **17**, 195–211 (2007).

47. M. A. Glozak, E. Seto, Histone deacetylases and cancer. *Oncogene* **26**, 5420–5432 (2007).

48. J. Gräff, L.-H. Tsai, The potential of HDAC inhibitors as cognitive enhancers. *Annu. Rev. Pharmacol. Toxicol.* **53**, 311–330 (2013).

49. C. L. Zhang, T. A. McKinsey, S. Chang, C. L. Antos, J. A. Hill, E. N. Olson, Class II histone deacetylases act as signal-responsive repressors of cardiac hypertrophy. *Cell* **110**, 479–488 (2002).

50. A. Nebbioso, V. Carafa, M. Conte, F. P. Tambaro, C. Abbondanza, J. Martens, M. Nees, R. Benedetti, I. Pallavicini, S. Minucci, G. Garcia-Manero, F. Iovino, G. Lania, C. Ingenito, V. Belsito Petrizzi, H. G. Stunnenberg, L. Altucci, c-Myc modulation and acetylation is a key HDAC inhibitor target in cancer. *Clin. Cancer Res. Off. J. Am. Assoc. Cancer Res.* **23**, 2542–2555 (2017).

51. S. Subramanian, S. E. Bates, J. J. Wright, I. Espinoza-Delgado, R. L. Piekarz, Clinical toxicities of histone deacetylase inhibitors. *Pharmaceuticals* **3**, 2751–2767 (2010).

52. X. Gao, L. Shen, X. Li, J. Liu, Efficacy and toxicity of histone deacetylase inhibitors in relapsed/refractory multiple myeloma: Systematic review and meta-analysis of clinical trials. *Exp. Ther. Med.* **18**, 1057–1068 (2019).

53. M. Packer, S. D. Anker, J. Butler, G. Filippatos, S. J. Pocock, P. Carson, J. Januzzi, S. Verma, H. Tsutsui, M. Brueckmann, W. Jamal, K. Kimura, J. Schnee, C. Zeller, C. Cotton, E. Bocchi, M. Böhm, D.-J. Choi, V. Chopra, E. Chuquiure, N. Giannetti, S. Janssens, J. Zhang, J. R. G. Juanatey, S. Kaul, H.-P. B.-L. Rocca, B. Merkely, S. J. Nicholls, S. Perrone, I. Pina, P. Ponikowski, N. Sattar, M. Senni, M.-F. Seronde, J. Spinar, I. Squire, S. Taddei, C. Wanner, F. Zannad, Cardiovascular and renal outcomes with empagliflozin in heart failure. *N. Engl. J. Med.* **383**, 1413–1424 (2020).

54. J. R. Teerlink, R. Diaz, G. M. Felker, J. J. V. McMurray, M. Metra, S. D. Solomon, K. F. Adams, I. Anand, A. Arias-Mendoza, T. Biering-Sørensen, M. Böhm, D. Bonderman, J. G. F. Cleland, R. Corbalan, M. G. Crespo-Leiro, U. Dahlström, L. E. Echeverria, J. C. Fang, G. Filippatos,

C. Fonseca, E. Goncalvesova, A. R. Goudev, J. G. Howlett, D. E. Lanfear, J. Li, M. Lund, P. Macdonald, V. Mareev, S. Momomura, E. O'Meara, A. Parkhomenko, P. Ponikowski, F. J. A. Ramires, P. Serpytis, K. Sliwa, J. Spinar, T. M. Suter, J. Tomcsanyi, H. Vandekerckhove, D. Vinereanu, A. A. Voors, M. B. Yilmaz, F. Zannad, L. Sharpsten, J. C. Legg, C. Varin, N. Honarpour, S. A. Abbasi, F. I. Malik, C. E. Kurtz, Cardiac myosin activation with omecamtiv mecarbil in systolic heart failure. *N. Engl. J. Med.* **384**, 105–116 (2020).

55. J. J. V. McMurray, M. Packer, A. S. Desai, J. Gong, M. P. Lefkowitz, A. R. Rizkala, J. L. Rouleau, V. C. Shi, S. D. Solomon, K. Swedberg, M. R. Zile, Angiotensin–neprilysin inhibition versus enalapril in heart failure. *N. Engl. J. Med.* **371**, 993–1004 (2014).

56. T. Knezevic, V. D. Myers, F. Su, J. Wang, J. Song, X.-Q. Zhang, E. Gao, G. Gao, M. Madesh, M. K. Gupta, J. Gordon, K. N. Weiner, J. Rabinowitz, F. V. Ramsey, D. G. Tilley, K. Khalili, J. Y. Cheung, A. M. Feldman, Adeno-associated virus serotype 9–driven expression of BAG3 improves left ventricular function in murine hearts with left ventricular dysfunction secondary to a myocardial infarction. *JACC Basic Transl. Sci.* **1**, 647–656 (2016).

57. C. Y. Chen, M. A. Caporizzo, K. Bedi, A. Vite, A. I. Bogush, P. Robison, J. G. Heffler, A. K. Salomon, N. A. Kelly, A. Babu, M. P. Morley, K. B. Margulies, B. L. Prosser, Suppression of detyrosinated microtubules improves cardiomyocyte function in human heart failure. *Nat. Med.* **24**, 1225–1233 (2018).

58. P. Robison, M. A. Caporizzo, H. Ahmadzadeh, A. I. Bogush, C. Y. Chen, K. B. Margulies, V. B. Shenoy, B. L. Prosser, Detyrosinated microtubules buckle and bear load in contracting cardiomyocytes. *Science* **352**, aaf0659 (2016).

59. D. Portran, L. Schaedel, Z. Xu, M. Théry, M. V. Nachury, Tubulin acetylation protects long-lived microtubules against mechanical ageing. *Nat. Cell Biol.* **19**, 391–398 (2017).

60. P. M. McLendon, B. S. Ferguson, H. Osinska, M. S. Bhuiyan, J. James, T. A. McKinsey, J. Robbins, Tubulin hyperacetylation is adaptive in cardiac proteotoxicity by promoting autophagy. *Proc. Natl. Acad. Sci. U.S.A.* **111**, E5178–E5186 (2014).

61. J.-Y. Lee, Y. Nagano, J. P. Taylor, K. L. Lim, T.-P. Yao, Disease-causing mutations in parkin impair mitochondrial ubiquitination, aggregation, and HDAC6-dependent mitophagy. *J. Cell Biol.* **189**, 671–679 (2010).

62. P. Guedes-Dias, J. de Proença, T. R. Soares, A. Leitão-Rocha, B. R. Pinho, M. R. Duchen, J. M. A. Oliveira, HDAC6 inhibition induces mitochondrial fusion, autophagic flux and reduces diffuse mutant huntingtin in striatal neurons. *Biochim. Biophys. Acta BBA - Mol. Basis Dis.* **1852**, 2484–2493 (2015).

63. M. Kaliszczak, E. van Hechanova, Y. Li, H. Alsadah, K. Parzych, H. W. Auner, E. O. Aboagye, The HDAC6 inhibitor C1A modulates autophagy substrates in diverse cancer cells and induces cell death. *Br. J. Cancer* **119**, 1278–1287 (2018).

64. M. Maddah, M. A. Mandegar, K. Dame, F. Grafton, K. Loewke, A. J. S. Ribeiro, Quantifying drug-induced structural toxicity in hepatocytes and cardiomyocytes derived from hiPSCs using a deep learning method. *J. Pharmacol. Toxicol. Methods* **105**, 106895 (2020).

Science Translational Medicine

Phenotypic screening with deep learning identifies HDAC6 inhibitors as cardioprotective in a BAG3 mouse model of dilated cardiomyopathy

Jin YangFrancis GraftonSara RanjbarvaziriAna BudanFarshad FarshidfarMarie ChoEmma XuJaclyn HoMahnaz MaddahKevin E. LoewkeJulio MedinaDavid SperandioSnahel PatelTim HoeyMohammad A. Mandegar

Screening to save sarcomeres

Loss-of-function mutations in *BAG3* are associated with dilated cardiomyopathy (DCM). Here, Yang and colleagues performed high-content phenotypic screening in human induced pluripotent stem cell–derived cardiomyocytes (iPSC-CMs) lacking *BAG3* expression. Using deep learning, they identified histone deacetylase (HDAC) and microtubule inhibitors as potential cardioprotective agents. HDAC6 inhibition reduced sarcomere damage in cells and protected against heart failure in BAG3 cardiomyocyte–specific knockout mice and mice harboring a mutation in *BAG3* linked to DCM. TYA-018, an HDAC6-specific inhibitor, reduced sarcomere damage and apoptosis and improved mitochondrial function in mice and human iPSC-CMs, supporting the translational potential of HDAC6 inhibition for DCM.

View the article online
https://www.science.org/doi/10.1126/scitranslmed.abl5654
Permissions
https://www.science.org/help/reprints-and-permissions

Use of this article is subject to the Terms of service